

Submission version: 15 October 2007

# A New Approach to the Study of Stellar Populations in Early-Type Galaxies: K-band Spectral Indices and an Application to the Fornax Cluster<sup>1</sup>

David R. Silva<sup>2</sup>

*National Optical Astronomy Observatory<sup>3</sup>*

*950 North Cherry Ave., Tucson, AZ, 85748, USA*

`dsilva@tmt.org`

and

Harald Kuntschner

*Space Telescope European Co-ordination Facility*

*Karl-Schwarzschild-Str. 2, D-85748 Garching bei München, Germany*

`hkuntsch@eso.org`

and

Mariya Lyubenova

*European Southern Observatory*

*Karl-Schwarzschild-Str. 2, D-85748 Garching bei München, Germany*

`mlyubeno@eso.org`

---

<sup>1</sup>Based on new observations performed at the European Southern Observatory, Cerro Paranal, Chile; ESO program 68.B-0674A and 70.B-0669A as well as archival data from ESO program 076.B-0457A and the SINFONI Science Verification dataset.

<sup>2</sup>Current assignment: Observatory Scientist, Thirty Meter Telescope, 2632 East Washington Blvd., Pasadena, CA, 91107, USA

<sup>3</sup>NOAO is operated by the Association of Universities for Research in Astronomy (AURA), Inc., under cooperative agreement with the National Science Foundation.

## ABSTRACT

The strong spectral features near  $2.2\ \mu\text{m}$  in early-type galaxies remain relatively unexplored. Yet, they open a tightly focused window on the coolest giant stars in these galaxies – a window that can be used to explore both age and metallicity effects. Here, new measurements of K-band spectral features are presented for eleven early-type galaxies in the nearby Fornax galaxy cluster. Based on these measurements, the following conclusions have been reached: (1) in galaxies with no signatures of a young stellar component, the K-band Na I index is highly correlated with both the optical metallicity indicator  $[\text{MgFe}]'$  and the central velocity dispersion  $\sigma$ ; (2) in the same galaxies, the K-band Fe features saturate in galaxies with  $\sigma > 150\ \text{km s}^{-1}$  while Na I (and  $[\text{MgFe}]'$ ) continues to increase; (3)  $[\text{Si/Fe}]$  (and possibly  $[\text{Na/Fe}]$ ) is larger in all observed Fornax galaxies than in Galactic open clusters with near-solar metallicity; (4) in various near-IR diagnostic diagrams, galaxies with signatures of a young stellar component (strong  $\text{H}\beta$ , weak  $[\text{MgFe}]'$ ) are clearly separated from galaxies with purely old stellar populations; furthermore, this separation is consistent with the presence of an increased number of M-giant stars (most likely to be thermally pulsating AGB stars); (5) the near-IR Na I vs.  $\sigma$  or  $\langle\text{Fe I}\rangle$  vs.  $\sigma$  diagrams discussed here seem as efficient for detecting putatively young stellar components in early-type galaxies as the more commonly used age/metallicity diagnostic plots using optical indices (e.g.  $\text{H}\beta$  vs.  $[\text{MgFe}]'$ ). The combination of these spectral indices near  $2.2\ \mu\text{m}$  with high *spatial* resolution spectroscopy from ground-based or space-based observatories promises to provide new insights into the nature of stellar populations in the central regions of distant early-type galaxies.

*Subject headings:* galaxies: abundances — galaxies: elliptical and lenticular, cD — galaxies: stellar content

## 1. Introduction

Understanding the stellar content of early-type galaxies is fundamental to understanding their star formation and chemical evolution history. Most early-type galaxies are too distant to resolve their individual stars with current technology, rendering the direct study of their stellar populations impossible. Thus, their stellar populations must be studied using indirect methods.

In recent decades, significant effort has gone into trying to better constrain the stellar contents for early-type galaxies using optical spectroscopic data. The most commonly studied features have been Ca I H and K  $0.38\ \mu\text{m}$ ,  $\text{H}\beta$ , Mg b  $0.52\ \mu\text{m}$ , Fe  $\mu\text{m}\ 0.53$ , Na  $0.82\ \mu\text{m}$ , and CaT  $0.86\ \mu\text{m}$ . Interpretation of all such spectral features is intrinsically complicated by their blended nature – each feature is really the super-position of many spectral lines, usually from several different elements, blurred together by the line-of-sight velocity dispersion within each galaxy. There is no way to overcome this problem – it must simply be taken into account during analysis. As population synthesis models have become more sophisticated and digital stellar libraries more complete, this problem has become more tractable over time.

Another challenge arises from the composite nature of galaxies: each observed feature is the luminosity-weighted integrated sum of that feature from all stars in the observed line-of-sight. Naturally, luminosity-weighted does not imply mass-weighted. A relatively small fraction of the mass can dominate the observed luminosity and mask the underlying stellar population (e.g. as happens during a starburst event within a pre-existing galaxy).

Even in relatively quiescent galaxies, light from stars at several important evolutionary stages contribute roughly equally to the observed spectral features between  $0.4 - 1\ \mu\text{m}$  range. Hence, a feature depth change could be due to (e.g.) a change near the (mostly) age-driven main-sequence turnoff or the (mostly) metallicity-driven red giant branch. The details can become quite complicated, as illustrated by the long standing controversy about whether observed changes in Balmer line strength arise from the presence of younger main sequence stars, more metal-poor main sequence stars, or an extended horizontal giant branch (for recent discussions of this debate, see Maraston & Thomas 2000 and Trager et al. 2005). A similar controversy surrounds Na  $0.82\ \mu\text{m}$  feature: is it driven by metallicity-driven red giant branch changes, initial mass function related differences in the relative number of cool dwarf and giant stars or both (e.g. Carter, Visvanathan, & Pickles 1986; Alloin & Bica 1989; Delisle & Hardy 1992)?

However, the properties of the RGB component can be isolated by observing in the K-band (centered near  $2.2\ \mu\text{m}$ ). At those wavelengths, cool giants near the tip of the first-ascent red giant branch (RGB) dominate the integrated light in old ( $\geq 3\ \text{Gyr}$ ) stellar populations. In combination with optical observations, K-band observations should facilitate the separation of MSTO and RGB light contributions. There are two possible complications to this scenario. First, a very young stellar population containing red supergiants will contribute a significant fraction K-band light. Fortunately, such a population is obvious from the presence of H II region emission lines at shorter wavelengths. Second, a somewhat older population ( $1 - 2\ \text{Gyr}$ , i.e. an intermediate-age population) may contain bolometrically bright carbon stars that can contribute a detectable amount of K-band light (see discussions in Silva & Bothun

1998a,b). Such a population may or may not be connected to increased  $H\beta$  strength.

Initial development of these ideas can be found in Silva et al. (1994), Mobasher & James (1996), James & Mobasher (1999), Mobasher & James (2000), all of whom focused on the CO 2.36  $\mu\text{m}$  feature. Origlia et al. (1997) observed a Si dominated feature at 1.59  $\mu\text{m}$  as well as CO dominated features. These observational studies were limited by small-format detectors to relatively low resolving powers and/or small wavelength ranges per observation. In the cases of Silva et al. and Origlia et al., only small, heterogeneous samples of galaxies were observed. A general conclusion of the James & Mobasher studies was that changes in CO strength between early-type galaxies in high-density and low-density regions were statistically consistent with different fraction contributions of intermediate-age AGB light and hence galaxies in low-density regions had younger luminosity-weighted mean ages. Origlia et al. argued that  $[\text{Si}/\text{Fe}]$  was super-solar in the four elliptical galaxies they observed.

To further develop these ideas and investigate the usefulness of other K-band spectral indices in the study of early-type galaxies, new data have been obtained for eleven E/S0 galaxies in the nearby Fornax cluster. Only measurements in the central regions of these galaxies are discussed here. In Section 2, the galaxy sample and its observations are discussed, while in Section 3 the data processing methodology is described. The measurement of spectral feature strength is explained in Section 4 while basic observation results are presented in Section 5. The broader astrophysical implications of our observational results are discussed in Section 6. A summary is provided at the end.

## 2. Observations

Long-slit spectroscopic data obtained with ISAAC at the ESO Very Large Telescope (VLT) have been combined with data obtained with SINFONI at the VLT to study a small sample of early-type galaxies in the nearby Fornax cluster. Details about the sample as well as the instrumental setups for these two instruments are presented in this section.

### 2.1. Samples

The full sample observed consists of eleven early-type galaxies in the nearby Fornax cluster, sub-divided into six elliptical galaxies and five S0 galaxies. The overall sample was selected to cover a significant range in luminosity weighted age, metallicity and mass. Basic galaxy properties are summarized in Table 1.

Optical long-slit spectroscopy is available for all observed galaxies (Kuntschner 2000, Kuntschner et al. 2002) allowing comparison between the K-band line-strength indices derived in this paper with optical indices. When compared to simple stellar population models, three galaxies (NGC 1316, NGC 1344 and NGC 1375) appear to have a significant contribution from young stars resulting in luminosity weighted ages between 1 and 3 Gyrs (see Figure 1). The remaining galaxies are consistent with being dominated by old stellar populations with a range in average metallicity.

Multi-color HST Advanced Camera for Survey images (courtesy of A. Jorden) of all the galaxies in our sample were inspected for the presence of dust. Three galaxies (NGC 1316, NGC 1344, and NGC 1380 – see details below) have clear central dust features. The other galaxies in our sample have no visible dust feature within the investigated aperture.

A few additional object specific remarks seem warranted:

*NGC 1316* – Fornax A, S0(3)pec. This galaxy has large scale, irregular, central dust features (based on inspection of HST-ACS images).

*NGC 1344* – this S0 galaxy contains morphological shells in its outer regions (Malin & Carter 1980) as well as optical spectral signatures of a younger central population (e.g. Kuntschner et al. 2002). Inspection of HST-ACS images reveals patchy dust within the central 5 arcsec. In combination, these characteristics suggest (1 – 2 Gyr) dynamical interaction or merger event that triggered a central star formation episode.

*NGC 1375* – Kuntschner (2000) concluded that the mean age of the central population of this S0 galaxy is significantly lower than for the other galaxies in our sample.

*NGC 1380* – contains a kinematically decoupled core (KDC) (Longo et al. 1994). It also contains an optically thick, well-organized central dust lane, easily visible in available HST images.

*NGC 1381* – this S0 galaxy contains X-bulge isophotal pattern, often attributed to a recent dynamical encounter or merger event.

*NGC 1399* – cD, E0

*NGC 1419* – this E0 galaxy has anomalously bright K-band surface brightness fluctuations (SBF) relative to its I-band surface brightness fluctuations, suggesting the presence of extended giant branches, perhaps due to the presence of an intermediate-age population (Mei et al. 2001; Liu, Graham, & Charlot 2002).

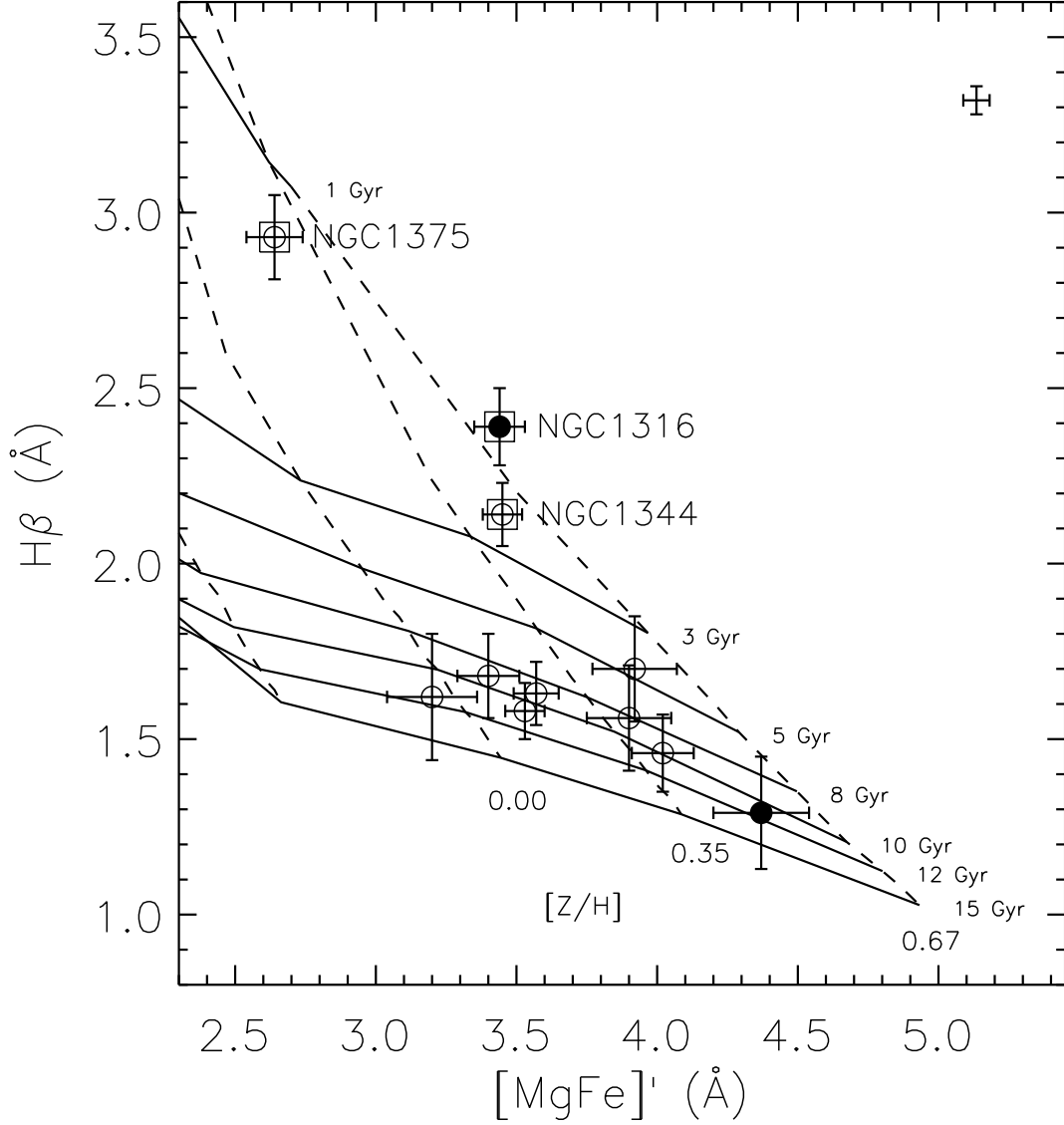


Fig. 1.—  $H\beta$  versus  $[MgFe]'$  age/metallicity diagnostic diagram. Overplotted are simple stellar population models for solar abundance ratios by Thomas, Maraston & Bender (2003). Solid and dashed lines show lines of constant luminosity weighted age and metallicity, respectively. Filled circles represent observations for NGC 1316 and NGC 1399 for which the IR indices were obtained with VLT-SINFONI and are extracted from a  $2 \times 3''$  aperture. For all other galaxies (open circles)  $1/8$  effective radius extractions are shown. Galaxies with a significant contribution of an intermediate age (1–2 Gyr) population are marked by open squares. The error bar in the upper right corner indicates the uncertainty in the transformation to the Lick/IDS system. For details see Section 3.3.

*NGC 1427* – this E4 galaxy also has anomalously bright K-band SBF (see NGC 1419 SBF references above). It also contains a KDC (D’Onofrio et al. 1995).

A small sample of Galactic open cluster stars were also observed. Their basic properties are summarized in Table 2. Cluster parameters (age, metallicity) and star photometry come from Houdashelt, Frogel, & Cohen (1992). Age has units of Gyr. Spectral types (SpT) have been assigned based on their  $J - K$  colors following Johnson (1966) for K giant stars and Lee (1970) for M giant stars. These stars have several roles: velocity dispersion templates, CO 2.36  $\mu\text{m}$  index comparisons, and small independent framework for interpreting K-band line strength variations as functions of basic atmospheric parameters. Each of these roles will be discussed in turn below.

Finally, several bright hot stars were observed to measure and correct the telluric absorption features in the K-band. B stars were selected by color from the Hipparcos Tycho catalog (ESA, 1997). In the spectral range of interest, these stars have no spectral features; therefore, that any observed features must be telluric absorption lines. In addition to color, proximity to the target objects and brightness were used as secondary selection criteria. The actual stars observed are listed in Table 3. The  $V$  magnitude and  $B - V$  color are from the Tycho catalog (ESA, 1997).

## 2.2. ISAAC observations

Most of the observations discussed in this paper were obtained at the ESO Very Large Telescope using the ISAAC near-IR imaging spectrometer mounted at one of the Nasmyth foci of the 8.2m UT1/Antu telescope. Galaxy observations were obtained in 2002 January and 2002 November. A summary observations log is given in Table 4. For each galaxy, the following information is provided: UT Date of observation, integration time per frame, number of frames, and total integration time. Since NGC 1380 and NGC 1404 were observed multiple times, each observation sequence is assigned a sequence identifier (A, B, C, ...).

ISAAC was used in short-wavelength spectroscopic mode at medium-resolution (SWS-MR). In this mode, the array used is a  $1024 \times 1024$  Hawaii Rockwell HgCdTe array with a spatial plate scale of  $0''.148 \text{ pix}^{-1}$ . A  $120 \times 1''$  slit was used. The dispersion and spectral resolution measured from our arc lamp data were  $1.21 \text{ \AA pix}^{-1}$  and  $7.7 \text{ \AA}$  (FWHM,  $R \simeq 2900$ ), respectively. The approximate wavelength range was  $2.12 - 2.37 \mu\text{m}$  but the central wavelength was always corrected for object redshift to ensure that all relevant spectral features were observed.

Galaxy observations were obtained using the standard nod-on-slit mode. At the start of

Table 1. Galaxy Sample

Galaxy	Type	$z$	$\sigma$ (km s <sup>-1</sup> )	R <sub>e</sub> maj ( $''$ )	R <sub>e</sub> min ( $''$ )	PA maj ( $^{\circ}$ )	R <sub>e</sub> extr. ( $''$ )	SNR	Note
(1)	(2)	(3)	(4)	(5)	(6)	(7)	(8)	(9)	(10)
NGC 1316	So(3)pec	0.0059	226	132.2	90.5	50	...	168	Fornax A; SINFONI data
NGC 1344	E5	0.0039	171	26.7	15.6	165	3.3	121	Type from RC3
NGC 1374	E0	0.0043	196	26.6	24.2	118	3.3	124	KDC
NGC 1375	S0(cross)	0.0025	70	24.0	9.3	91	3.0	48	Central starburst
NGC 1379	E0	0.0044	138	23.9	23.3	182	2.9	78	...
NGC 1380	S0/a	0.0063	213	52.4	26.6	7	3.4	213	...
NGC 1381	S0(9)(boxy)	0.0057	169	23.5	8.0	139	2.9	135	...
NGC 1399	E0	0.0048	360	134.1	120.8	110	...	111	cD; SINFONI data
NGC 1404	E2	0.0065	221	26.0	23.0	157	157	280	...
NGC 1419	E0	0.0071	128	9.4	9.3	188	1.2	111	K-band SBF outlier
NGC 1427	E4	0.0046	186	39.2	27.1	76	4.9	104	K-band SBF outlier, KDC

Note. — Notes: Galaxy types (column 2) were extracted from Ferguson (1989) while redshifts (column 3) are taken from the NASA Extragalactic Database (NED) – original redshift references: (da Costa et al. 1998), D’Onofrio et al. (1995), Graham et al. (1998) and de Vaucouleurs et al. (1991). Central velocity dispersions (column 4) are taken from our own measurements of the ISAAC and SINFONI data (see Sections 3.1.4 and 3.2). The values for the effective radii (columns 5 and 6) were taken from Caon et al. (1994) and derived from the RC3 for NGC 1344. The position angle of the major axis (column 7) was taken from the RC3 and de Carvalho et al. (1991). The  $1/8 R_e$  extraction radius which was used to extract a central spectrum for the ISAAC observations is given in column 8. Empirical SNR estimates for the extracted spectra are given in column 9 (see Section 3.1 for details). Comments are given in column 10.



Table 2. Galactic open cluster stars

Cluster (1)	Age (2)	[Fe/H] (3)	Star (4)	$V - K$ (5)	$J - K$ (6)	SpT (7)
NGC 2204	2.8	−0.38	1146	5.71	1.12	M4
			3304	3.10	0.79	K3
			3325	3.84	0.94	M0.5
			4132	5.03	1.11	M3.5
NGC 2477	1.0	−0.02	1069	4.07	0.95	M1
			$\lambda$	2.96	0.71	K3
			2117	4.18	0.96	M2.5
			6053	2.81	0.68	K2
NGC 2506	3.5	−0.52	2401	3.65	0.91	K5
			4228	4.07	0.99	M1

Table 3. ISAAC telluric correction stars

Telluric Star (1)	Target (2)	$V$ (3)	$B - V$ (4)
Tycho2 7034 01323	Fornax galaxies	6.07	−0.11
Tycho2 5942 02406	NGC 2204	5.29	−0.19
Tycho2 7645 03250	NGC 2477	6.13	−0.17
Tycho2 5425 00772	NGC 2506	7.87	−0.14

Table 4. ISAAC Galaxy Observations Log

UT Date	Galaxy	$\tau$ (secs)	Frames	Total $\tau$ (secs)	PA	SeqID
(1)	(2)	(3)	(4)	(5)	(6)	(7)
2002 Jan 02	NGC 1404	500	6	3000	89.45	A
2002 Jan 14	NGC 1404	500	6	3000	...	B
2002 Jan 14	NGC 1404	500	6	3000	...	C
2002 Nov 12	NGC 1404	500	6	3000	...	D
2002 Nov 13	NGC 1404	500	6	3000	...	E
2002 Nov 13	NGC 1380	400	8	3200	89.45	A
2002 Nov 13	NGC 1380	400	8	3200	...	B
2002 Nov 12	NGC 1380	400	8	3200	...	C
2002 Nov 12	NGC 1344	400	8	3200	164.45	...
2002 Nov 13	NGC 1374	400	8	3200	89.45	...
2002 Nov 12	NGC 1375	400	8	3200	89.45	...
2002 Nov 13	NGC 1379	400	8	3200	89.45	...
2002 Nov 13	NGC 1381	400	8	3200	138.45	...
2002 Nov 12	NGC 1419	400	8	3200	89.45	...
2002 Nov 12	NGC 1427	400	8	3200	77.45	...

Table 5. SINFONI Galaxy Observations Log

UT Date	Galaxy	$\tau$ (secs)	O+S Frames	Total $\tau$ (secs)	SeqID
(1)	(2)	(3)	(4)	(5)	(6)
2004 Nov 25	NGC 1399	300	4+4	1200	B
2004 Nov 26	NGC 1399	300	4+4	1200	C
2004 Nov 26	NGC 1399	300	4+4	1200	D
2004 Nov 26	NGC 1399	300	4+4	1200	E
2005 Oct 13	NGC 1316	600	3+1	1800	A
2005 Oct 13	NGC 1316	600	4+2	2400	B

each observational sequence, the galaxy was centered on the slit near one end and a individual integration was executed. The galaxy was then moved approximately  $60''$  towards the other end of the slit where two more integrations were executed. The galaxy was then returned to the original slit position where another integration was obtained. This ABBA pattern was repeated a number of times, resulting in multiple individual two-dimensional spectroscopic images. Including time for telescope offsetting and array readout, each sequence took roughly one hour to execute.

After each set of galaxy sequences was completed, telluric standard Tycho2 7034 01323 was observed (see Table 3) at five different positions along the slit. At each position, a short ( $\leq 10$  secs) integration was obtained. At the end of the telluric integrations, a XeAr lamp-on/lamp-off sequence was obtained followed by a quartz lamp-on/lamp-off sequence. The spectrograph setup was not changed during the entire galaxy-standard-lamps sequence, ensuring that the grating did not move. Thus, each star-lamp sequence had the same central wavelength as the corresponding galaxy sequence. This is critical for proper correction of telluric features, dispersion, and array pixel-to-pixel response.

On various dates, stars from the following open clusters were observed: NGC 2204 (2002 November 12), NGC 2477 (2001 December 23), and NGC 2506 (2002 November 13). The actual stars observed are listed in Table 2. Each star was observed at five (5) positions along the slit. At each position, a short ( $\leq 10$  secs) integration was obtained. After each set of cluster star observations, a telluric standard was observed, followed by arc and flat lamp observations (as described above). The exact telluric standards observed are listed in Table 3.

As part of the VLT calibration program, calibration data was also obtained during the day following each set of observations. These data include observations of quartz and arc lamps (for flat-field and wavelength dispersion corrections) as well as dark frames with the same detector integration times (DITs) as the night-time science observations. For this project, the daytime quartz and arc lamps were not useful due to grating angle positioning inaccuracy.

### 2.3. SINFONI observations

Observations of NGC 1316 (Fornax A) and NGC 1399 (the central cD galaxy) were obtained with SINFONI, a near-IR integral field unit (IFU) spectrograph mounted at the Cassegrain focus of VLT UT4 (Yepun). A spatial scale of the  $0.1''$  scale was used, corresponding to a total field of view of approximately  $3'' \times 3''$ . The spectra cover the wavelengths

between  $1.95 - 2.4 \mu\text{m}$  at  $2.45 \text{ \AA}/\text{pix}$ . The spectral resolution is  $6.1 \text{ \AA}$  FWHM ( $R \simeq 3700$ ).

NGC 1399 was observed 2004 November 25 and 29 during the SINFONI Science Verification program (Eisenhauer et al. 2003; Bonnet et al. 2004). The NGC 1316 data come from the ESO Science Archive (Program 076.B-0457A, PI Ralf Bender). The original observations were made on 2005 October 13. Details of these observations are given in Table 5.

NGC 1399 was observed in a sequence OSSOOSO (O = object integration, S = sky/background integration) to enable accurate background correction. NGC 1316 was observed with a slightly different pattern – OSOOSO. As with the ISAAC observations discussed above, telluric and velocity template standard stars were observed periodically. The former were hot stars while the latter covered the range K5III to M1III.

### 3. Data Processing

#### 3.1. ISAAC data reduction

Data processing was done using a combination of shell scripts, `eclipse` (Devillard 1997), and IRAF<sup>1</sup>.

##### 3.1.1. Quartz and Arc Lamps

As described above, each ISAAC observing sequence consists of a set of galaxy or cluster star observations followed immediately by associated telluric star and lamp exposures. The lamps exposures were processed first. The resultant flat-field and XeAr arc lamp frames were used in turn to process their associated telluric star and galaxy or cluster star sequences.

A raw flat-field frame was constructed by subtracting the lamp-off exposure from the lamp-on exposure to remove thermal background and dark current. The difference frame was used to define the illuminated region of the ISAAC SW detector (the entire detector is not illuminated in SWS mode). The difference frame was trimmed to remove the unilluminated part. The trimmed frame was then collapsed in the spatial dimension into a one-dimensional vector. A one-dimensional polynomial was fit to this vector. This polynomial was then divided into every row of the original background-corrected flat-field frame. The

---

<sup>1</sup>The Image Reduction and Analysis Facility (IRAF) is distributed by the National Optical Astronomy Observatories (NOAO), which are operated by the Association of Universities for Research in Astronomy, Inc. (AURA) under contract with the National Science Foundation (NSF).

resultant frame is suitable for removing pixel-to-pixel sensitivity variations. These flat-field frames obtained immediately after all telluric sequences are preferred to evening or morning flats since tests demonstrated that such so-called daytime calibrations did not accurately remove fringing. This is presumably due to grating re-positioning imprecision.

The XeAr exposures were processed by first subtracting the arc-off frame from the arc-on frame, again to remove any background illumination not associated with the XeAr lamps. A two-dimensional wavelength dispersion correction was derived, using low-order polynomials in both dimensions.

### *3.1.2. Telluric Correction Star Observations*

For each telluric absorption correction star sequence, the five individual frames were first trimmed to correspond to the illuminated part of the detector (see above) and then divided by their associated flat-field. A background+dark frame was determined by median combining the individual flattened exposures. This background frame was then subtracted from those exposures. The five flat-field and background corrected frames were summed into a single frame. A spectral tilt correction was determined from the resultant frame. Spectral tilt and wavelength dispersion corrections were then applied to the summed, flat-field corrected frame. The five individual spectra were extracted and averaged into a single spectrum using a sigma-clipping algorithm for bad pixel rejection. This combined spectrum was used to produce two things: a normalized telluric absorption line correction spectrum and a instrument sensitivity correction.

Building the normalized telluric correction spectrum started by fitting a one-dimensional bi-cubic spline to the telluric star spectrum. Care was taken to reject high outliers (e.g. cosmic rays, bad pixels) but not too many low outliers (likely to be the telluric absorption features of interest). The derived vector was divided back into the original spectrum to normalize it and remove the continuum shape.

This bi-cubic spline fit was then re-used to determine an instrument sensitivity curve. Since the color of the telluric stars is known from the Hipparcos catalog, a reasonable estimate of their effective temperature can be made. Furthermore, since these are hot stars, we know that their continuum in the K-band is well approximated by the Rayleigh-Jeans part of the blackbody spectrum associated with their effective temperature. By computing the appropriate blackbody curve in the relevant wavelength range and then dividing it by the bi-cubic spline fit (i.e. a representation of the observed stellar continuum), the instrument sensitivity function can be estimated. Of course, this is not an absolute correction – but an

absolute correction is not necessary for the spectral line strength measurements described below.

### 3.1.3. *Cluster Star Observations*

Cluster star sequences were processed into single combined spectra in a similar manner as telluric star sequences. At that point, the combined spectrum of each star was divided by its associated normalized telluric absorption line correction spectrum. To remove the instrument response signature, the telluric corrected cluster star spectrum is then multiplied by the instrument sensitivity function.

To achieve the optimal telluric absorption line correction, it was typically necessary both to shift the telluric star spectrum in the dispersion direction (usually by less than 1 pixel) and scale it (usually by a few percent) before the division. The physical cause of the physical shift in the dispersion direction is unclear. However, the need to scale is simply due to the slight changes in airmass and time between object and telluric correction standard observations. It is also clear that the strength of every telluric absorption feature in this wavelength window is not changing in concert. Thus, the telluric correction is not perfect at all wavelengths. In principle, a more sophisticated correction process is possible. In practice, the current level of correction is good enough for this application.

The final processed spectra for all observed cluster stars are shown in Figure 2.

### 3.1.4. *Galaxy Observations*

The main technical goal of this paper is to make accurate line strength measurements in the central regions of our target galaxies. However, in the future, the radial line strength gradients will also be studied. Since each AB galaxy observation is only separated by  $\sim 100''$ , a simple AB subtraction (i.e. the typical procedure in the near-IR) could cause inaccurate dark and background correction in the lower surface brightness parts of the galaxy luminosity profiles. Therefore, a procedure derived from the processing of *optical* long-slit spectra was applied.

The basic data processing challenge is shown in Figure 3 where a central  $3''$  diameter extraction of NGC 1404 (sequence D; see Table 1) is shown at three stages: before background correction, after background correction but before telluric absorption line correction, and after all processing. One of the major advantages of ISAAC over other near-IR spectrometers is the ability to use a high-enough spectral resolution to resolve telluric features so that they

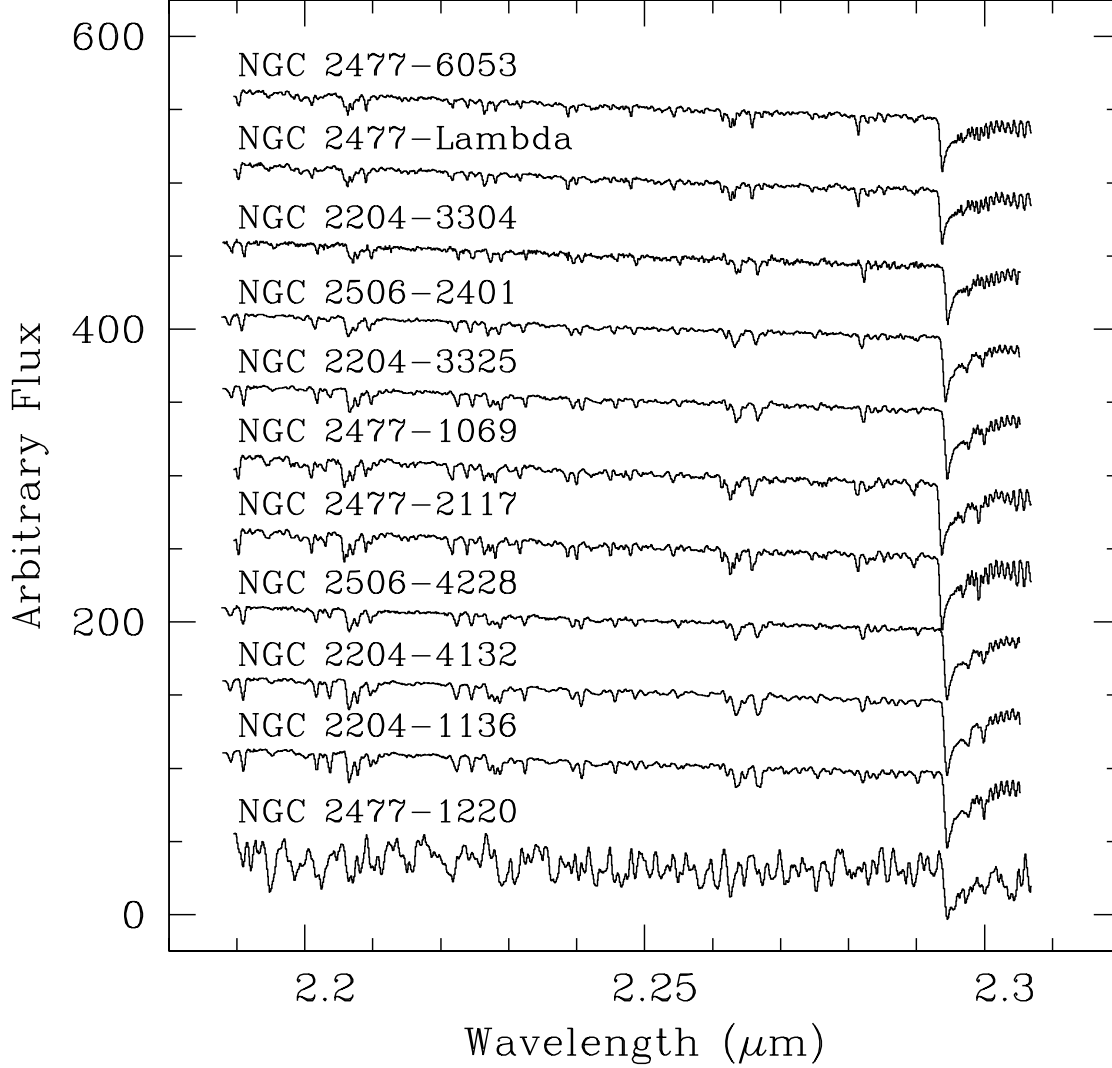


Fig. 2.— Galactic Open Cluster Stellar Spectra – Final spectra for all the stars listed in Table 2. Each spectrum was normalized to 100 at  $2.25 \mu\text{m}$  and then offset by a fixed amount for illustration purposes. The spectra are ordered (top to bottom) by increasing  $J - K$  color (hence, decreasing effective temperature). Note how the CaI  $2.207 \mu\text{m}$  and NaI  $2.265 \mu\text{m}$  atomic features as well as the CO  $2.36 \mu\text{m}$  molecular feature increase in depth with decreasing effective temperature. Star NGC 2477-1220 is a carbon star and not discussed further in this paper.

can be accurately removed.

As shown in Table 1, each galaxy observation consists of a series of 6 or 8 individual exposures taken in ABBA sequences. To begin, each galaxy frame was trimmed and the appropriate median dark frame was subtracted. Following the advice of the *ISAAC Data Reduction Guide* (available on-line from the ESO ISAAC Web page), electronic ghosting was removed using the `eclipse` recipe *isaacp ghost*.

Recall that each galaxy sequence had an associated telluric+lamp sequence. As described in the telluric star processing section above, each telluric+lamp sequence was processed into a series of calibrations: flat-field, two-dimensional wavelength dispersion solution, spectral tilt correction, normalized telluric absorption correction vector, and instrument sensitivity function. After electronic ghost correction, each individual galaxy frame was divided by this flat-field and then geometrically rectified using the derived dispersion and spectral tilt solutions. In short, the galaxy sequence and its associated telluric star are calibrated using the same frames and vectors.

A slit illumination correction was applied next. Since twilight sky exposures were not available, the correction function had to be reconstructed from the actual observations. In each individual galaxy observation, the spatial dimension can be divided into a galaxy sub-section and a sky sub-section. For each AB pair, the sky sub-section is on opposite sides of the slit center. The A and B sky sub-sections were extracted and merged into a single A+B sky frame, after applying a small additive offset to the B sky sub-section to align it better with the A sky sub-section. This offset is caused by temporal changes in the background between the A and B exposures. This process was repeated for all A and B galaxy exposures on a given night. The resultant frames were then scaled to a common mean value and averaged using a sigma clipping bad pixel rejection scheme. That average sky frame was collapsed in the dispersion direction into a one-dimensional vector. A nightly illumination correction function was derived by fitting a second-order bi-cubic spline to that vector and normalizing the result. This illumination correction was then divided into all galaxy frames from that night.

The next step was to remove the background. The standard procedure would be to select a radial position dominated by the background, determine the mean background at this position, and subtract that value at every pixel in the spatial dimension. As applying this procedure to the current dataset did not produce satisfactory results, an alternative two-step approach was developed. First, for each AB pair, an illumination corrected A+B sky frame was produced as described above and then subtracted from the parent A and B frames. Second, on each frame, the standard procedure was applied. This two-step procedure produced a much better background correction than the standard procedure alone.



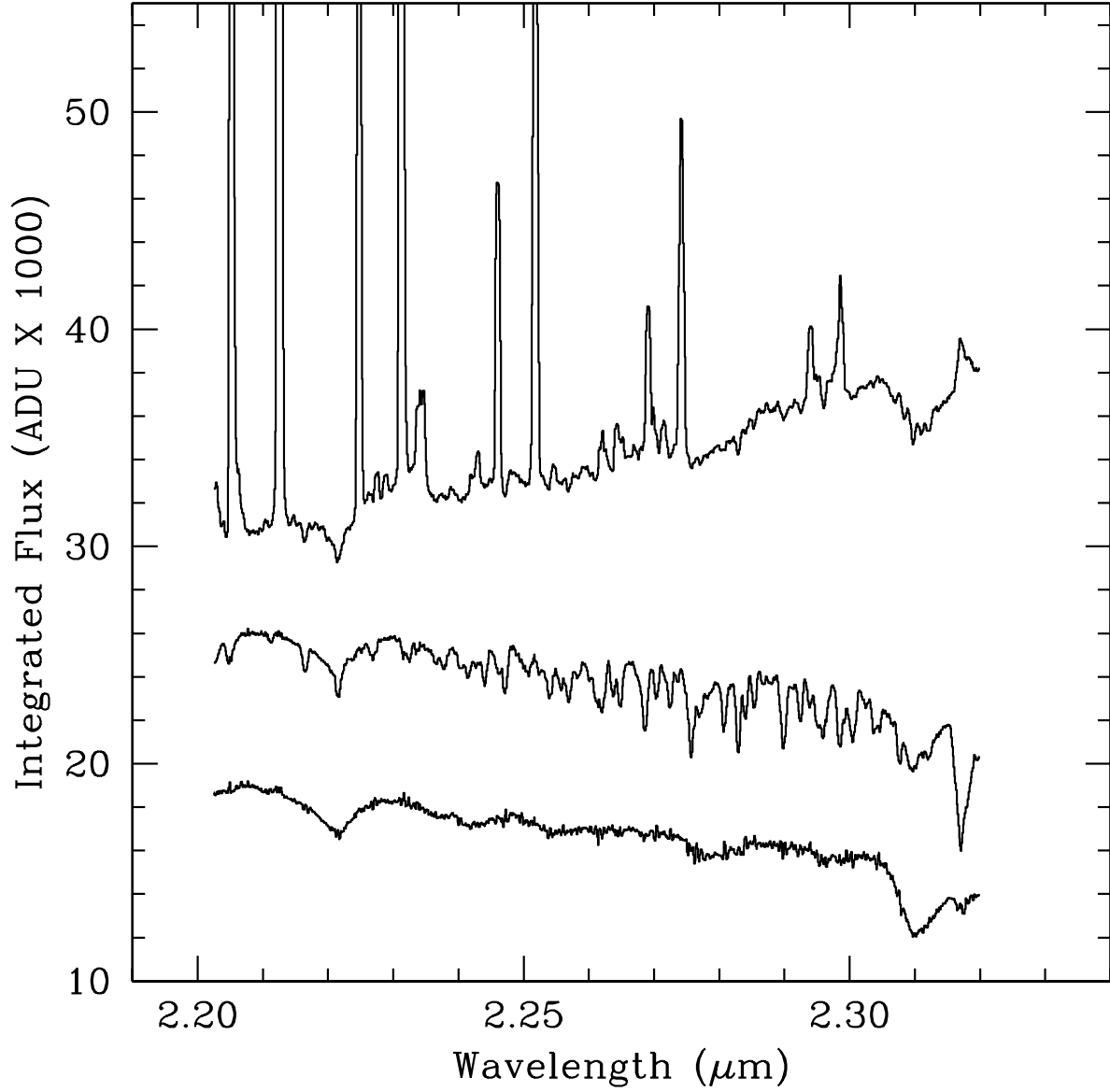


Fig. 3.— Galaxy Processing Example – A central  $3''$  diameter extraction of NGC 1404 (Sequence D, see Table 1) are shown (from top-to-bottom): before corrections for dark current, background, telluric absorption, and instrument sensitivity; after dark current and background (emission) correction; and after correction for telluric absorption and instrument sensitivity. No correction for redshift has been applied. The top and bottom spectra are shown at their observed relative integrated flux levels. Some of the telluric emission lines have integrated fluxes greater than 80 000 ADU. The middle and bottom spectra have been separated by an arbitrary additive offset; otherwise, they would lie on top of each other.

Each background corrected frame was then corrected for telluric absorption lines, using the associated normalized telluric absorption correction vector. As described in the cluster star processing section above, small shifts in the dispersion direction as well as small multiplicative scaling were necessary to achieve the best possible correction.

Finally, the six (or eight) individual frames combined into a single frame. Before this combination, the individual frames were shifted to a common center (defined by the maximum intensities in the galaxy spectra) with sub-pixel accuracy using linear interpolation. Given the pixel scale ( $0''.148 \text{ pix}^{-1}$ ) vs. the natural seeing (estimated to be  $\sim 0''.8$  from the profiles of the telluric star observations), alignment accuracy is not critical. The frames were then scaled to a common median value at a fixed point in the galaxy spectra and then averaged using a sigma-clipping rejection scheme. The final step was to multiple each combined frame by the sensitivity function derived from its associated telluric standard (see above).

Basic post-processing data quality can be assessed from Figure 4 shows the central  $3''$  diameter extraction for all the galaxies observed in 2002 November. The spectra are ordered by velocity dispersion ( $\sigma$ ) which corresponds essentially to decreasing signal-to-noise per pixel due to decreasing central intensity. The sharper spectral features seen in the galaxies with lower  $\sigma$  are intrinsic to the galaxies – they are not caused by less accurate telluric line correction in these fainter galaxies.

To first order, measurement repeatability can be assessed from Figure 5 where the central  $3''$  diameter extraction of NGC 1380 and NGC 1404 are shown from two and three different nights, respectively. In the case of NGC 1404, these observations were separated by months. Clearly, the gross properties of the extracted spectra are the same. Repeatability of line strength measurements is discussed in the next section.

The central spectra used for the measurement of spectroscopic features were extracted within a radius corresponding to  $1/8 R_e$  at the observed position angle for each galaxy (see also Tables 1 and 4). For each extracted spectra, an empirical signal-to-noise ratio (SNR) was derived following Stoeck et al. (2007) and listed in Table 1.

From these extracted spectra, recession velocities and velocity dispersions were measured using the penalized Pixel-Fitting method (pPXF) developed by Cappellari & Emsellem (2004). For simplicity, purely Gaussian line shapes were assumed. The resulting measurements are needed as input for the line-strength determinations (see Section 4). The velocity dispersions are tabulated in Table 1 and are used throughout this paper. Errors on the kinematics parameters are calculated within the code based on error frames which are produced by our data reduction scripts. See also Section 3.3 for further analysis of the kinematic errors.

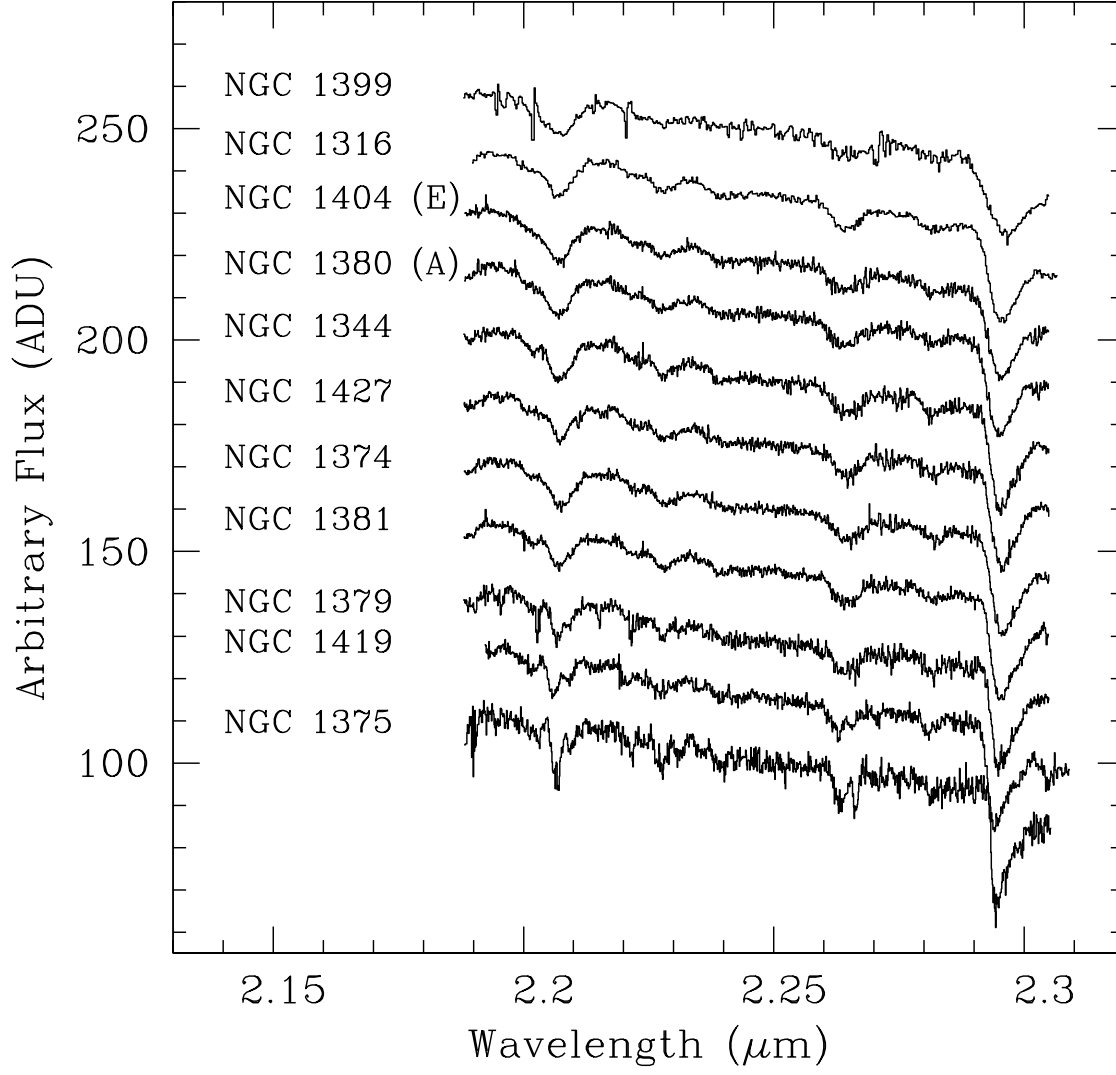


Fig. 4.— Central  $3''$  diameter extractions for all galaxies ordered by decreasing central velocity dispersion from top to bottom (see Table 1).

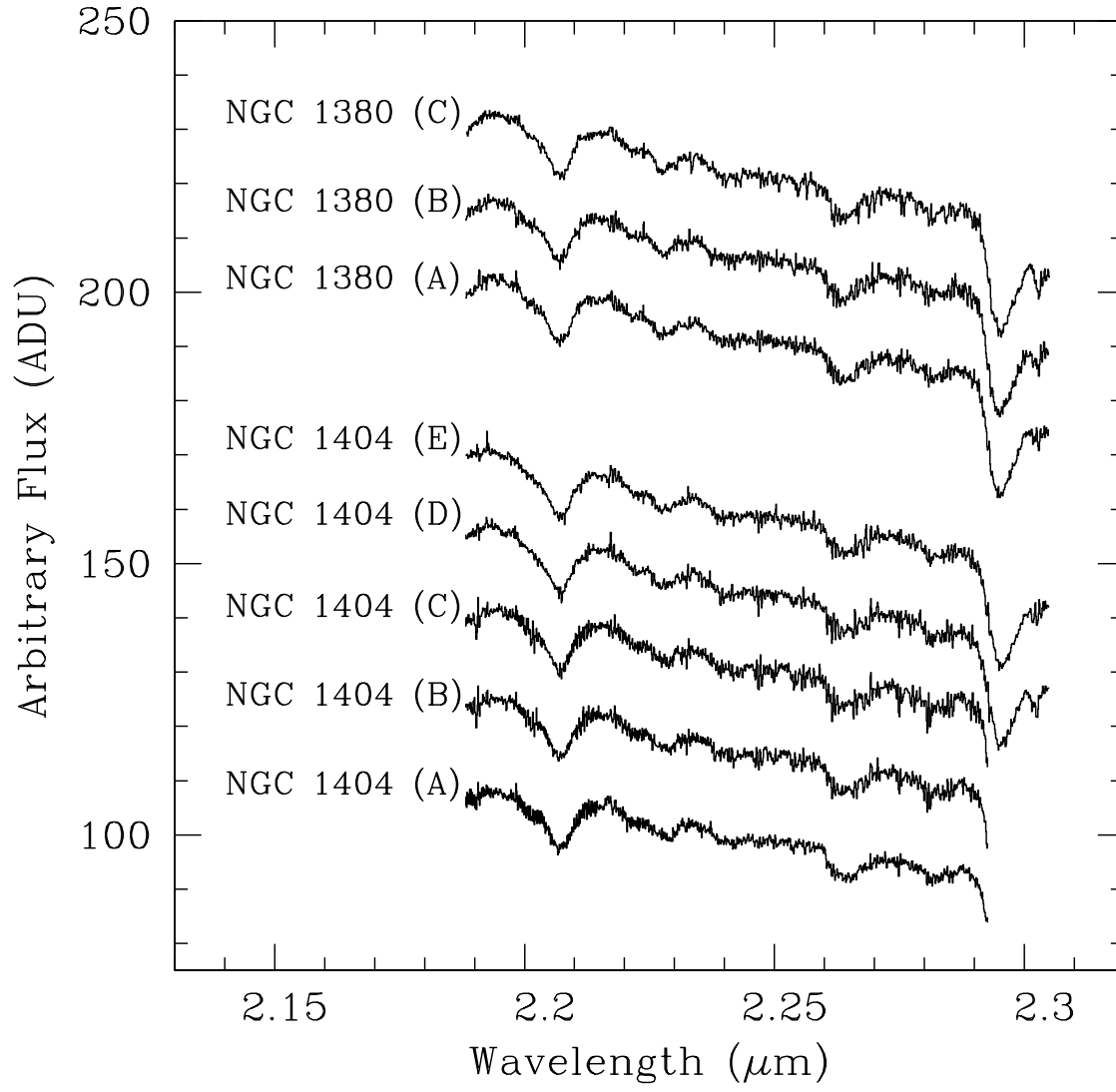


Fig. 5.— Central 3'' diameter extractions for 1404(A-E) and 1380(A-B).

### 3.2. SINFONI data reduction

SINFONI observations of NGC 1316 and NGC 1399 were processed and calibrated using the SINFONI Pipeline (v. 1.6). The pipeline transforms raw science data frames into flat-field corrected, wavelength calibrated and background subtracted three-dimensional data cubes for the galaxies and the calibration stars, including the extraction of one-dimensional spectrum from the central 10 pixels of the observed galaxies and stars.

For NGC 1399, the telluric stars were solar-type. In order to obtain a telluric correction spectrum, the star spectra were divided by a scaled and Gaussian broadened solar spectrum. This step removes intrinsic stellar features and continuum shape. A correction for telluric features was then applied as described above for the ISAAC observations.

The NGC 1316 telluric stars were hotter B stars that have no prominent spectral features in the wavelength range of interest. The telluric correction spectrum was obtained by dividing the stellar spectrum by a scaled black body spectrum with the same temperature as the star. A correction for telluric features was then applied as described above for the ISAAC observations.

The individual data cubes for the two galaxies were then combined to achieve better signal-to-noise ratios. The four NGC 1399 data cubes were averaged using a sigma-clipping pixel reject algorithm. Since there were only two NGC 1316 observations, pixel reject during combination was not possible.

Since the field-of-view of the VLT-SINFONI observations was limited to approximately  $3 \times 3''$ , an extraction radius of  $1/8 R_e$  is not possible. Therefore, a slit of  $2 \times 3''$  was extracted from the datacube to match the slitwidth of the optical data for these galaxies (see Section 3.3). As for the ISAAC data, the recession velocities and velocity dispersions were measured with pPXF (see also Table 1) and errors determined from noise statistics.

### 3.3. Optical data processing

The long-slit spectroscopy from Kuntschner (2000) and Kuntschner et al. (2002, NGC 1344) was used to extract a central spectrum for each galaxy. The extraction aperture was set to match the effective area covered on the sky by the central ISAAC data. The position angle of the ISAAC observations was set to agree with the optical data. Due to the rather different slit widths involved (ISAAC  $1''$ , optical Fornax data  $2''.3$  and  $2''$ ) the extraction ranges vary. For the two galaxies observed with VLT-SINFONI (NGC 1316 and NGC 1399) the extraction aperture is limited by the field-of-view of SINFONI. In order to best match the optical and

near-IR data we extracted a central  $2''.3 \times 3''$  slit from the optical observations.

Again pPXF was used to derive recession velocities and velocity dispersions. Good fits were achieved for all galaxies but NGC 1375 where the formal result was  $\sigma = 32 \text{ km s}^{-1}$ . This is well below the resolution limit of the optical Fornax data (Kuntschner 2000;  $4.1 \text{ \AA}$  FWHM,  $R \simeq 1300$ ) and is therefore unreliable. In this paper, the velocity dispersion derived from the higher spectral resolution ISAAC data was adopted and assigned a relatively large error of  $\pm 20 \text{ km s}^{-1}$  to reflect the uncertainty of this procedure.

A comparison between optical and near-IR measurements of the central velocity dispersions is shown in Figure 6. The determinations are in good agreement with each other for all galaxies, including the two galaxies with significant contributions of young stellar populations (NGC 1344 and NGC 1316). Taking the difference between the optical and near-IR measurements as a guideline for our true errors (including differences in seeing and remaining aperture differences) we conclude that our internal velocity dispersion error needs to be scaled by a factor of 2.2. In the following analysis and figures, these conservative scaled errors are used.

## 4. Line Strength Measurements

### 4.1. Spectral Feature Definitions

The spectral features investigated are listed in Table 6. For all but one feature, absorption-line strength is measured as equivalent width via indices, where a central feature bandpass is flanked to the blue and red by pseudo-continuum band-passes. This method is identical to what is used to measure optical Lick indices (Worthey et al. 1994). The index definitions for Na I and Ca I were taken from Frogel et al. (2001). Revised Fe I A, Fe I B, and Mg I index definitions were used since earlier definitions (e.g. Förster-Schreiber 2000) did not incorporate continuum band definitions optimized for galaxy spectra with significant velocity broadening. In order to measure the strength of the  $^{12}\text{CO}(2,0)$  absorption we use the definitions of Frogel et al. 2001 which provide four pseudo-continuum bandpasses to the blue of the CO feature and none to the red. Therefore the continuum used to derive the equivalent width is an extrapolation from the blue wavelength region in contrast to the Lick indices where the continuum is based on an interpolation between two flanking bandpasses.

The feature bandpasses of all measured indices are illustrated in Figure 7 which shows how the absorption features change as a function of temperature in red giant stars. The spectra shown (taken from Wallace & Hinkle 1997) are similar in spectral resolution to our spectra (see Figure 2 above). It is important to remember that all of these features are

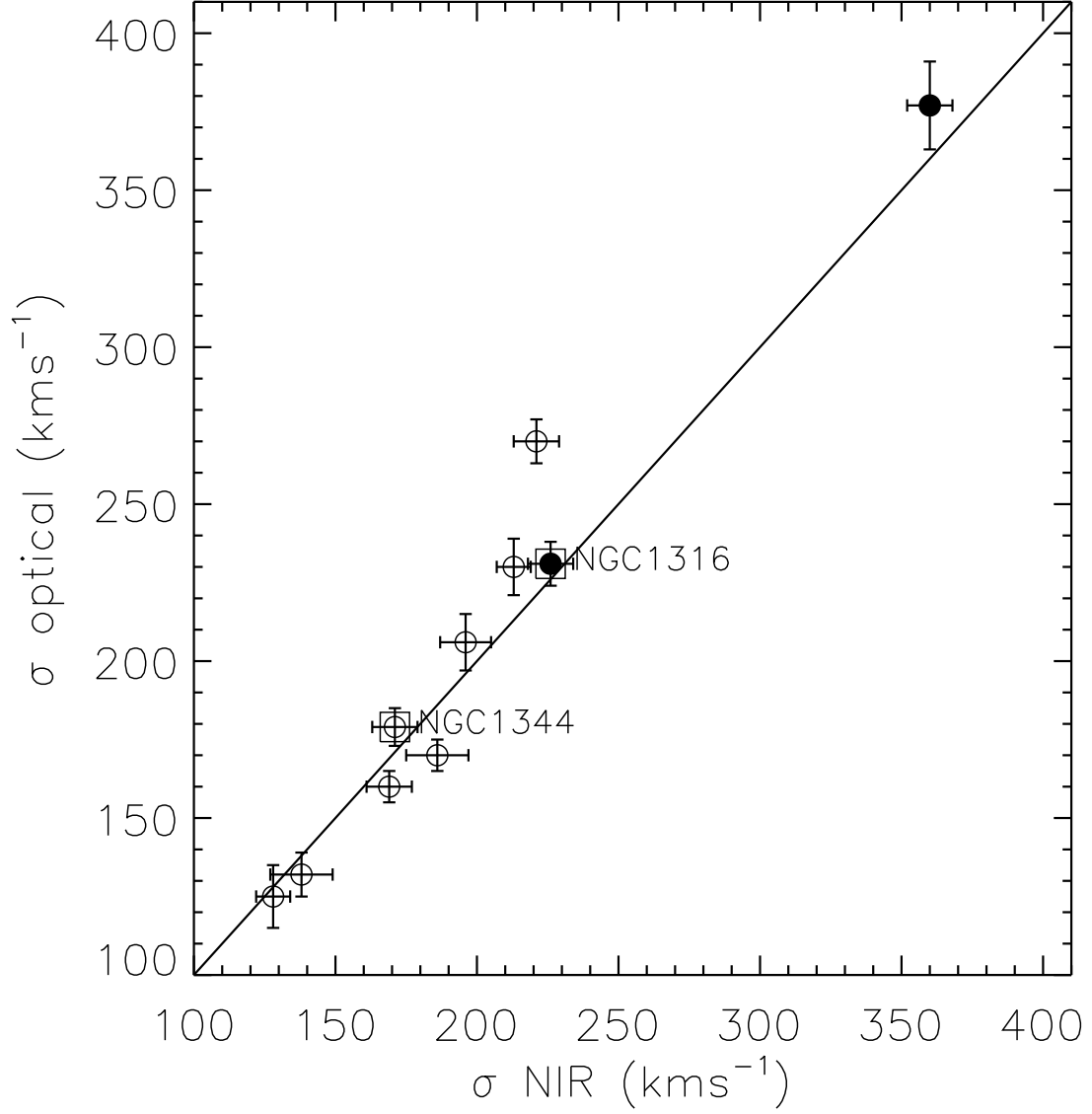


Fig. 6.— Comparison of our velocity dispersions determinations between the near-IR data and the optical spectroscopy. Central extractions correspond to  $1/8 R_e$ , except for NGC 1316 and NGC 1399 ( $\sigma \simeq 360 \text{ km s}^{-1}$ ) where a fixed aperture of  $2 \times 3''$  was used. NGC 1375 is not shown – see text for details.

really blends of distinct atomic and molecular features, especially at cooler temperatures. This point is richly illustrated by the  $R \sim 40\,000$  spectra presented in Wallace & Hinkle (1996) (see, in particular, their Figures 2 and 3 for the Ca I and Na I features, respectively).

## 4.2. Measurement Procedure

In order to allow a meaningful comparison between observations of stars and galaxies (with different internal dynamics) to themselves and to population models, index measurements need to be carefully calibrated to a common system. There are generally three effects to account for: (a) the differences in spectral resolution of the instruments used to obtain the index measurements; (b) the internal velocity broadening of galaxies and (c) possibly small systematic offsets caused by continuum shape differences (see also Kuntschner 2000).

The resolution of our ISAAC observations ( $6.9\text{\AA}$  FWHM, or  $R \simeq 3300$ ) was adopted as the nominal resolution. The VLT-SINFONI spectra were broadened to match this resolution before the measurement of the line-strengths indices. The observed spectrum of a galaxy is the convolution of the integrated spectrum of its stellar population(s) by the instrumental broadening and line-of-sight velocity distribution (LOSVD) of the stars. These effects typically broaden the spectral features, in general reducing the observed line-strength compared to the intrinsic values. In order to compare the index measurements for galaxies we calibrate the indices to zero velocity dispersion and our nominal resolution.

Although non-Gaussian deviations from the LOSVD can have significant effects on the LOSVD correction of indices (see e.g., Kuntschner 2004), in this study, only the first moments,  $v$  and  $\sigma$ , are considered. This is a reasonable approximation for central spectra studied in this study since expected non-Gaussian deviations in this region are negligible.

Observations of K and M giants are used to determine the corrections for each index. These spectra are a reasonable match to the observed galaxy spectra; however, once stellar population models become available the corrections should be re-derived. By broadening the stellar spectra to velocity dispersions of up to  $400\text{ km s}^{-1}$  in steps of  $20\text{ km s}^{-1}$  a median correction factor is computed for each index, i.e.:

$$C_j(\sigma) = I_j(\sigma = 0)/I_j(\sigma), \quad (1)$$

and  $I_j$  is the median index measured from the stars convolved with the LOSVD given in brackets. A LOSVD corrected index is then  $I_j^{corr} = C_j(\sigma) \times I_j^{raw}$ . The actual correction functions computed here are shown in Figure 8.



Table 6. Index definitions

Index	Blue pseudo-continuum	Central bandpass	Red pseudo-continuum	Units	Source
Na I	21910 – 21966	22040 – 22107	22125 – 22170	Å	Frogel et al. 2001
Fe I A	22133 – 22176	22250 – 22299	22437 – 22497	Å	This paper <sup>a</sup>
Fe I B	22133 – 22176	22368 – 22414	22437 – 22497	Å	This paper <sup>a</sup>
Ca I	22450 – 22560	22577 – 22692	22700 – 22720	Å	Frogel et al. 2001
Mg I	22700 – 22720	22795 – 22845	22850 – 22874	Å	This paper <sup>a</sup>
Index	Continuum bands		Feature bandpass	Units	Source
<sup>12</sup> CO(2,0)	22300 – 22370, 22420 – 22580, 22680 – 22790, 22840 – 22910		22910 – 23020	Å	Frogel et al. 2001

Note. — Notes: (a) Our new index definitions were inspired by Förster-Schreiber (2000) but are not identical to the definitions used in that paper.

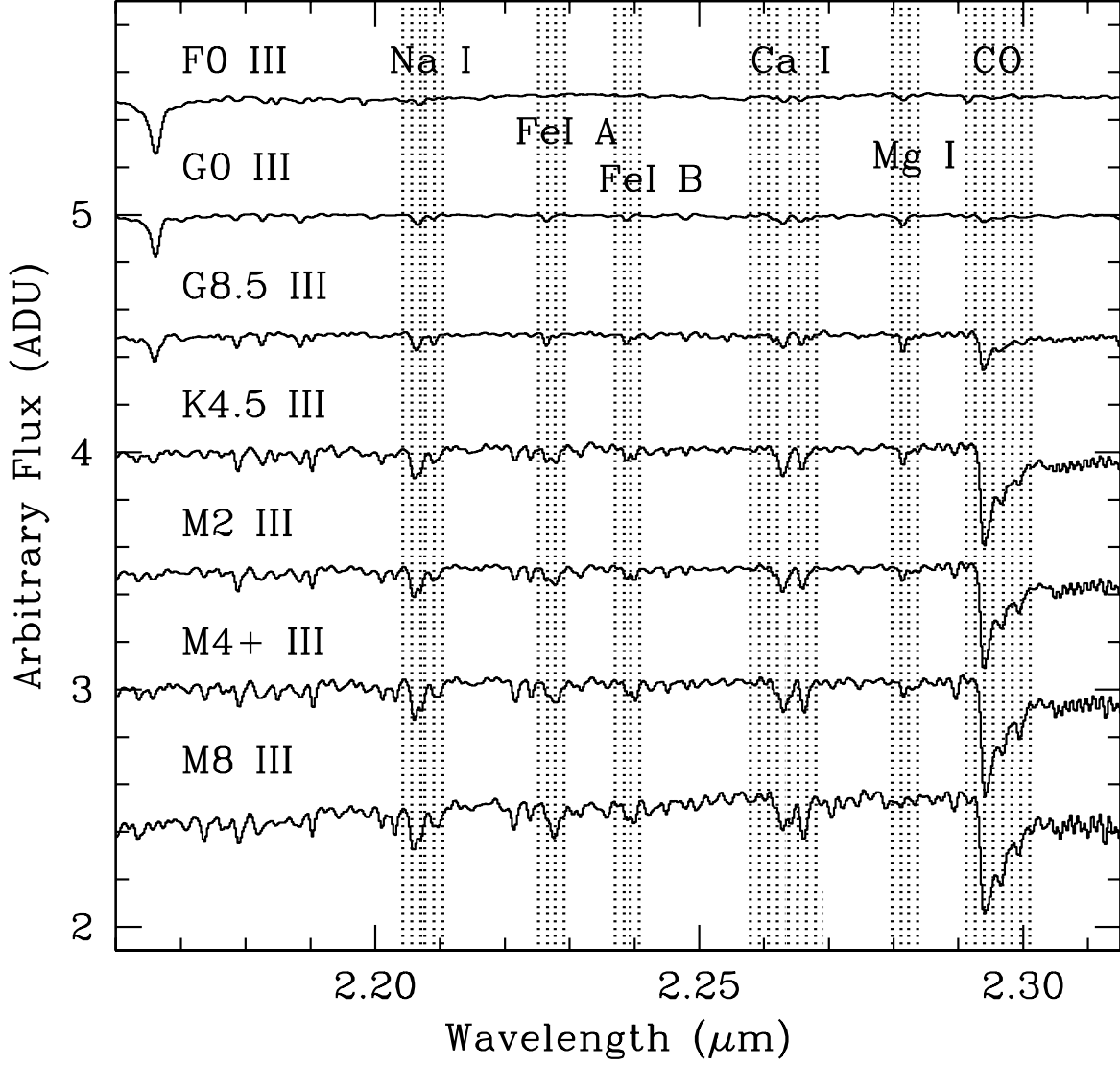


Fig. 7.— Spectral Features Defined – Using near-IR spectra from Wallace & Hinkle (1997), the on-band regions of the spectral features defined in Table 6 are shown. The Wallace & Hinkle spectra and the new spectra described here have similar spectral resolution (see Figure 2).

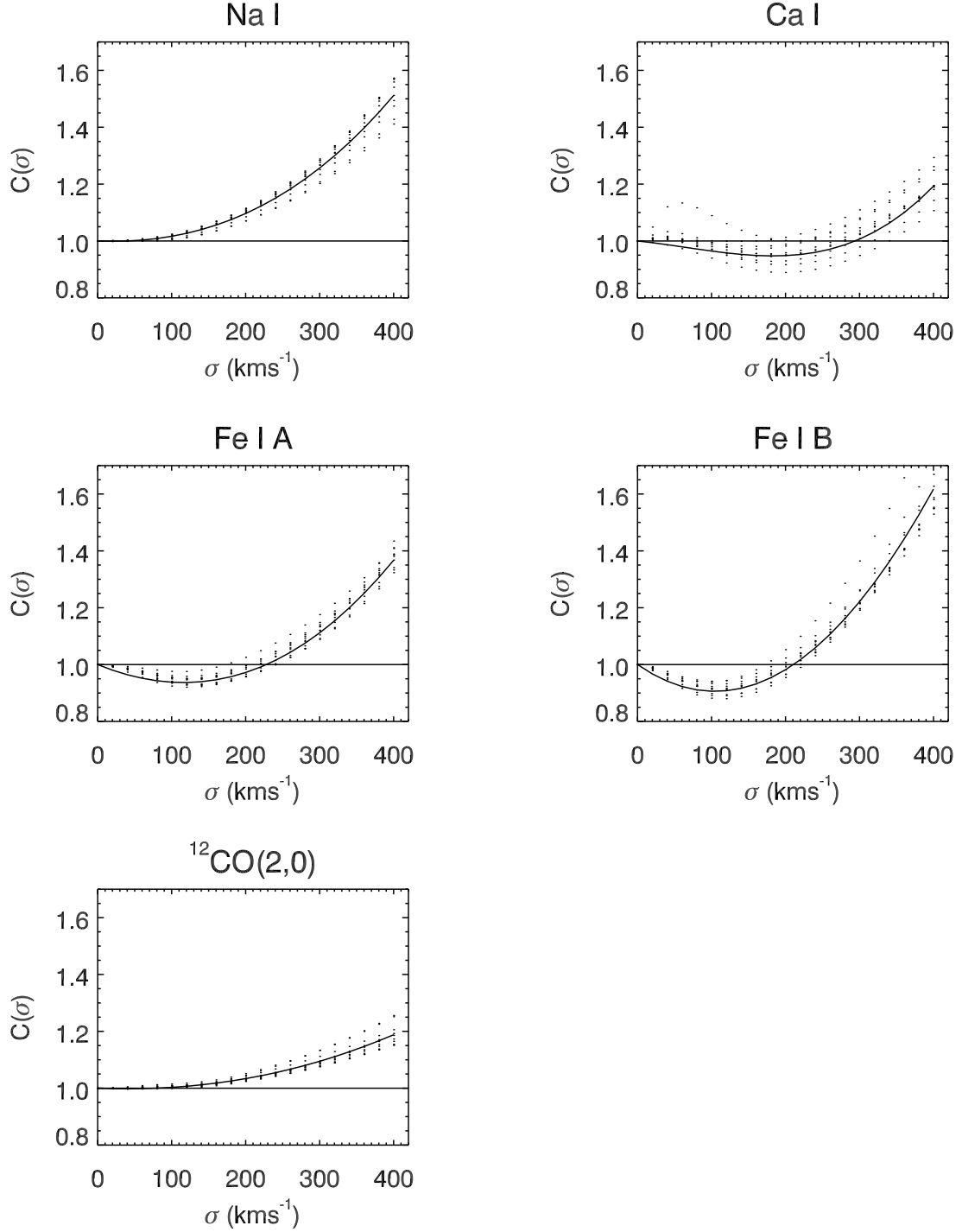


Fig. 8.— Line of sight velocity distribution (LOSVD) corrections for near-IR indices. Dots represent individual stars broadened to different velocity dispersions. The solid line is a 3rd order polynomial fit to the data and is used to apply the LOSVD corrections. See text for further details.

For the optical data the velocity dispersion corrections from Kuntschner (2004) were used. The errors on the line-strength indices are evaluated by using error estimates from the spectra and taking into account the errors from the LOSVD correction procedure. The optical data was calibrated to the Lick/IDS system. For a more detailed description of the procedure see Kuntschner (2000).

Multiple ISAAC observations of NGC 1380 and NGC 1404 allow us to constrain possible systematic errors in our line strength measurements. Figure 9 is plotted with the same y-axis range as Figure 13 but with an smaller  $\sigma$  range. For the Na I, Ca I, Fe I A and Fe I B indices our error estimate are comparable to the observed repeatability uncertainty. However, in the case of the CO index the repeatability uncertainty is significantly larger and we adopt the internal dispersion of the NGC 1380 and NGC 1404 measurements ( $0.3 \text{ \AA}$ ) as the formal uncertainty for all subsequent analysis.

Line-strength indices can be sensitive to continuum shape calibration errors. In particular index definitions spanning a wide wavelength range are prone to suffer from this. In our study the wide band-pass of the CO index (see Table 6) falls in this regime and we consider this to be the explanation for the larger spread between repeat observations.

## 5. Results

### 5.1. Cluster stars

The origin and behavior of the Na I, Ca I, and CO features as a function of effective temperature in K and M giant stars has been extensively reviewed and discussed by Ramírez et al. (1997) and Förster Schreiber (2000) (who also studied the Fe and Mg features). Most of the stars used in those studies were field stars with bright apparent magnitudes and hence drawn from a narrow metallicity range biased towards solar metallicity. The behavior of the Na I, Ca I, and CO features as a function of metallicity for Galactic globular cluster K and M giants has been investigated by Frogel et al. (2001). The metallicity range of that study covers both the metallicity range of the clusters investigated here, as well as the luminosity-weighted mean metallicities of the Fornax early-type galaxies.

In Figure 10, the index strength (in  $\text{\AA}$ ) for all six measured spectral features is plotted against  $J - K$  color as tabulated by Houdashelt, Frogel, & Cohen (1992) (hereafter HFC92) for the open cluster stars listed in Table 2. These stars are all K or M giant stars. In this context, redder  $J - K$  implies cooler effective temperature and lower surface gravity. Within a single cluster, it is reasonable to assert that this lower effective temperature is not metallicity-driven. As previously shown in the studies discussed above, all features increase

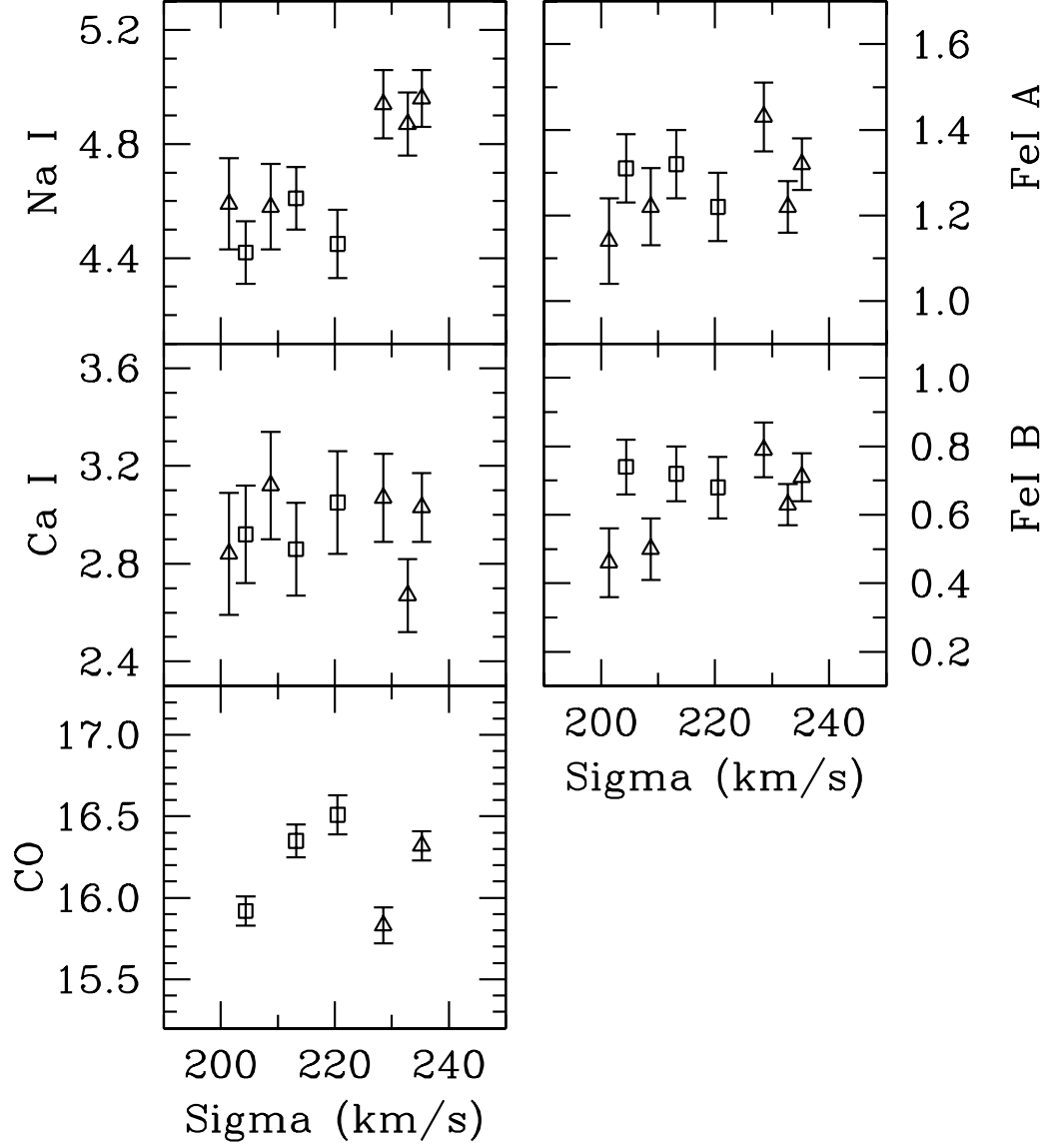


Fig. 9.— Repeated ISAAC Line Strength Measurements. Repeated measurements for NGC 1380 (*open squares*) and NGC 1404 (*open triangles*) are shown. See text for further information.

in depth with redder color (and hence decreasing  $T_{eff}$ ) except Mg I, which appears to have a more or less constant value for each cluster regardless of effective temperature (see also Förster Schreiber 2000).

The CO, Fe I A, and Fe I B features are highly correlated with  $J - K$  and show no dependency on cluster metallicity. For the CO feature, this behavior is consistent with the results of Frogel et al. (2001) over a similar cluster metallicity range. No analogous study exists for the Fe features. However, as shown in Figure 11, the Fe I A and Fe I B index strengths are highly correlated with each other. Hence, it is convenient to define a mean index:  $\langle \text{Fe I} \rangle = (\text{Fe I A} + \text{Fe I B}) / 2$  that has a smaller formal uncertainty than either individual Fe index alone. This mean index  $\langle \text{Fe I} \rangle$  is used throughout the rest of this paper.

As anticipated by the results of Frogel et al. (2001), at a given  $J - K$  (i.e.  $T_{eff}$ ), giant stars in more metal-rich clusters have stronger Na I and Ca I features. The Mg feature (not included in the Frogel et al. study) appears to have similar behavior, although we note again that within a given cluster (and hence for a given metallicity), the Mg feature strength is approximately constant with  $J - K$ .

In Figure 12, various combinations of K-band line indices are shown. Na I,  $\langle \text{Fe I} \rangle$  and CO are highly correlated with each other (linear correlation coefficient,  $r > 0.9$ ). There is a hint that Na I is stronger in the solar-metallicity stars at equivalent CO and  $\langle \text{Fe I} \rangle$  than in the more metal-poor stars. It is much clearer that at equivalent Na I and  $\langle \text{Fe I} \rangle$ , Ca I is stronger in the solar-metallicity stars than in the more metal-poor stars.

## 5.2. Fornax galaxies

In Figure 13, central K-band spectral feature measurements are plotted against central velocity dispersion measured from our data. Mg I has not been shown here (and is ignored for the rest of the paper) because this line is relatively weak and a reliable velocity dispersion correction could not be derived. Relative to the stellar spectral line strengths shown in Figure 10, the galaxy measurements (except Na I) fall in the middle of the ranges of the stellar measurements. Taken at face value, this is consistent with saying that the luminosity-weighted spectral type for all these galaxies is similar to a solar-metallicity M0 III star.

For most of our galaxies, the Na I feature is stronger than measured in any of our observed stars or any of the field disk giants observed by Ramirez et al. (1997). Only the supergiants in the Förster Schreiber have such strong Na features. The unlikely possibility of a supergiant-dominated population can be ruled out by CO index values that are completely

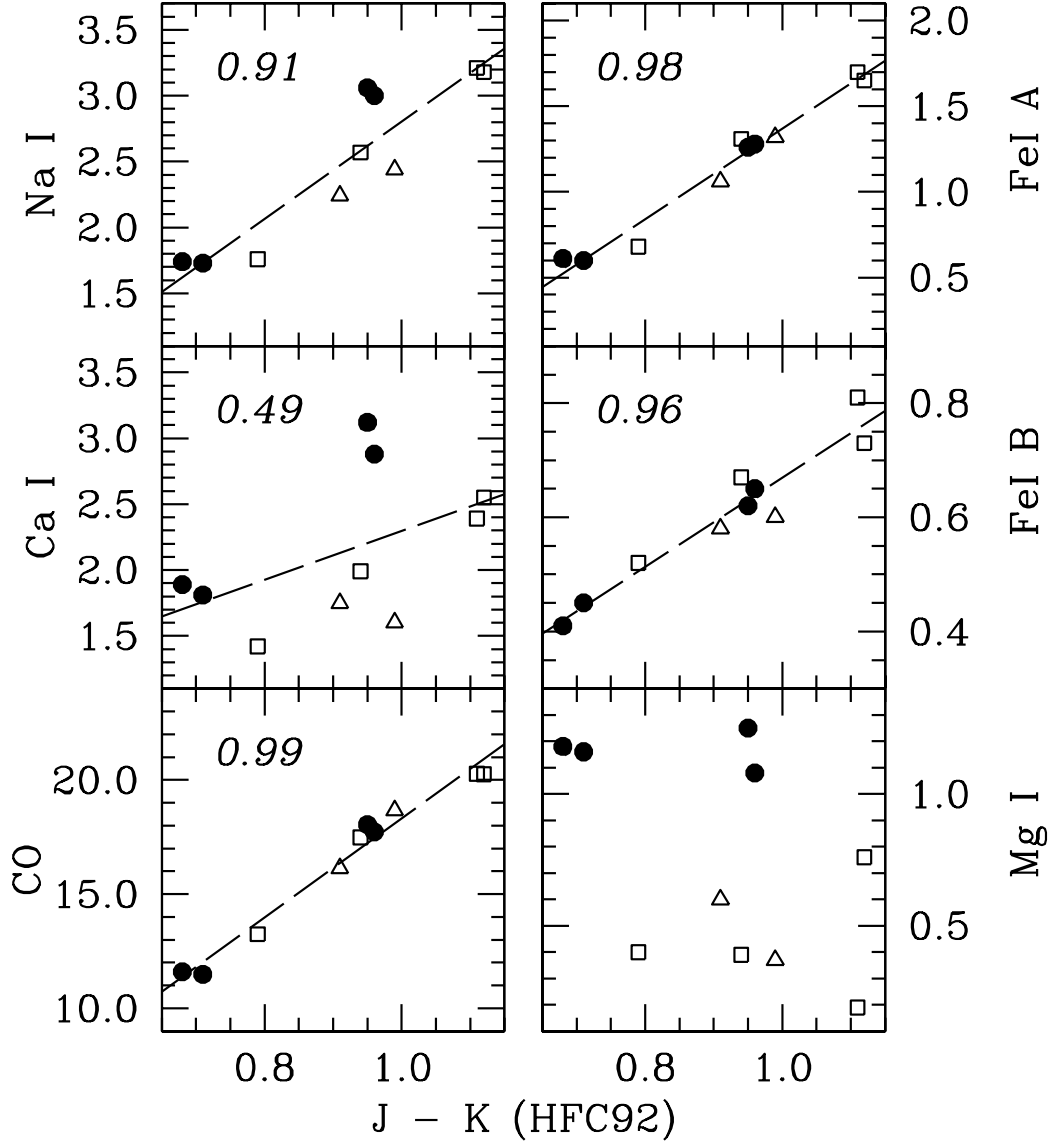


Fig. 10.— Cluster Star Line Strength vs.  $J - K$ . The strengths of all six measured K-band spectral features plotted against  $J - K$  color as tabulated by Houdashelt, Frogel, & Cohen (1992). The *filled circles* are NGC 2477 stars ( $[\text{Fe}/\text{H}] = -0.02$ ), the *open squares* are NGC 2204 stars ( $[\text{Fe}/\text{H}] = -0.38$ ), and the *open triangles* are NGC 2506 stars ( $[\text{Fe}/\text{H}] = -0.52$ ). The typical random uncertainty is smaller than the symbols, while the typical HFC92 color uncertainty is 0.02 mag. The *dashed line* in each panel is the unweighted linear least-squares fit between index strength and color. Linear correlation coefficients are given in each panel. Mg I appears to be constant within a cluster (or rather metallicity); hence, no global trend with color has been derived.

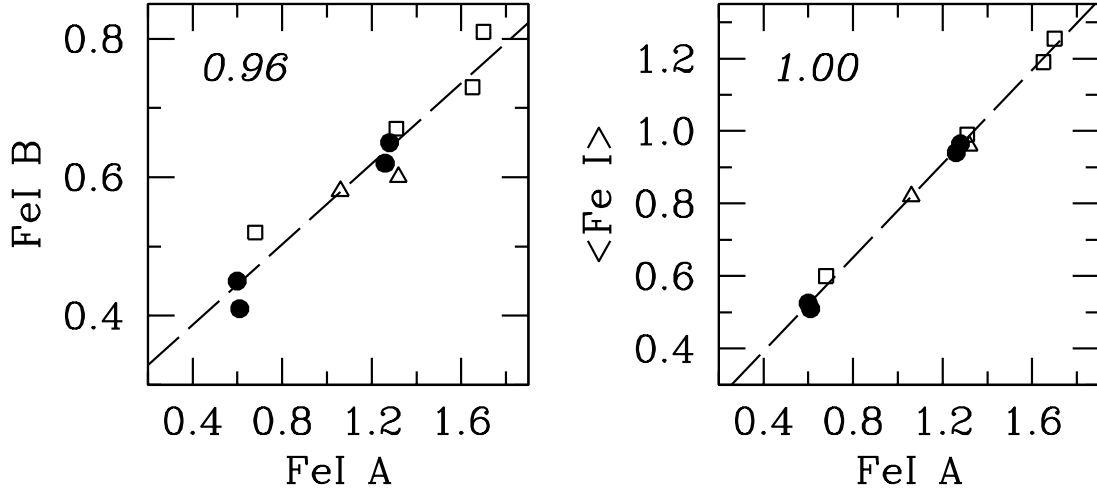


Fig. 11.—  $\langle \text{FeI} \rangle$  Definition. Since FeI A and FeI B strengths are highly correlated (*left panel*), it is convenient to define a mean index  $\langle \text{FeI} \rangle = (\text{FeI A} + \text{FeI B}) / 2$ . The symbols and dashed line are explained in Figure 10. The linear correlation coefficient for each panel is written in the upper left corner.



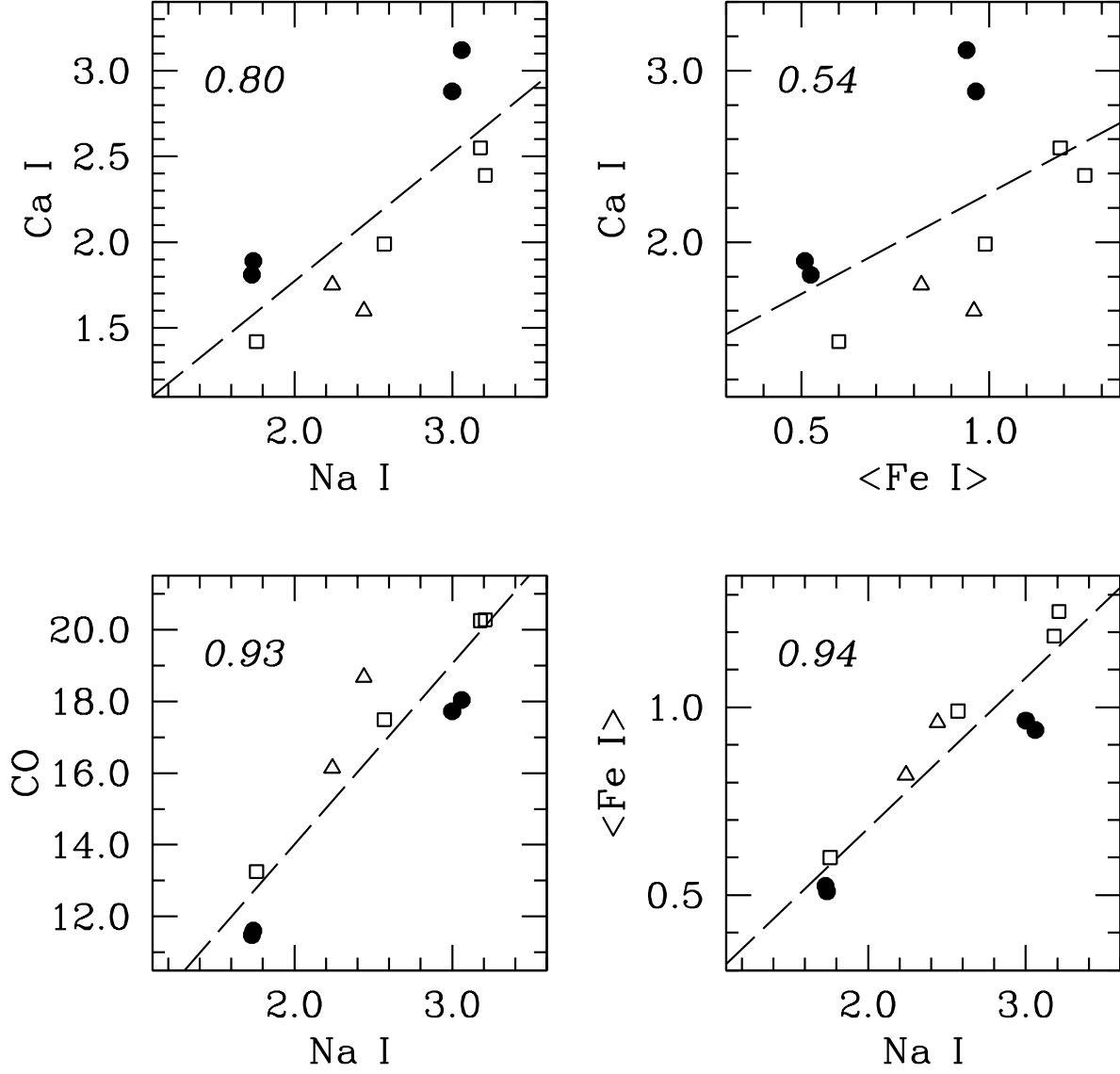


Fig. 12.— Cluster Star Line Strength vs. Line Strength. The symbols are explained in Figure 10. The dashed lines are the unweighted linear regression fits. The linear correlation coefficient for each relationship given in the upper left corner of each panel.

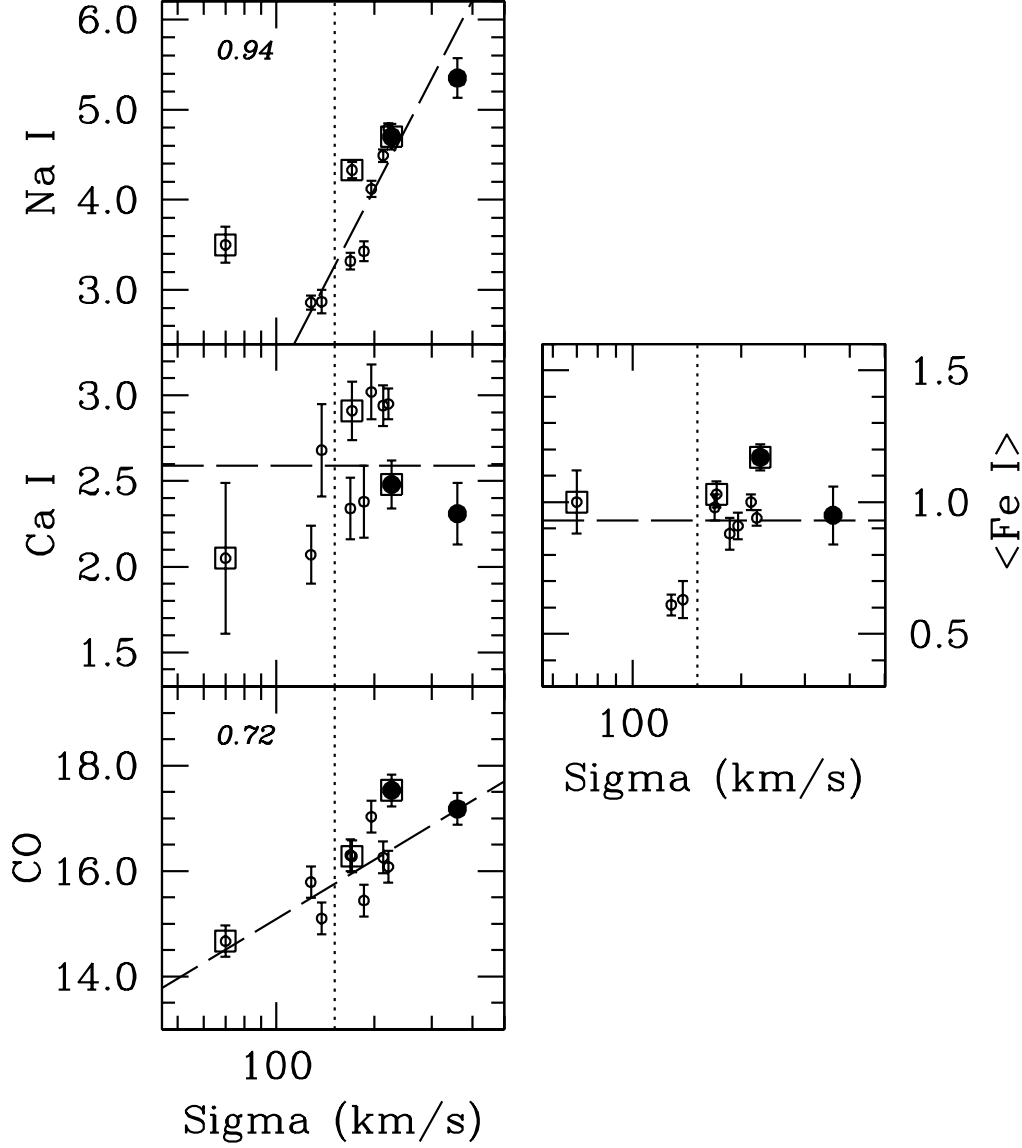


Fig. 13.— Fornax E/S0 Line Strength vs. Central Velocity Dispersion - the index strength plotted against central velocity dispersion ( $\sigma$ ) as measured from our K-band spectra. Individual ISAAC measurements for NGC 1380 and NGC 1404 have been averaged into mean values. The galaxies with young stellar components (NGC 1316, NGC 1344, and NGC 1375) are marked with *open squares*. Values derived from SINFONI observations (NGC 1316 and NGC 1399) are indicated by *filled circles*. The *slanted dashed lines* in Na I, Ca I, and CO panels are the unweighted linear regression fits for the purely old galaxies (i.e. without NGC 1316, NGC 1344, or NGC 1375). The linear correlation coefficient for each fit is shown. The *vertical dashed line* indicates  $\sigma = 150 \text{ km s}^{-1}$ . In the Ca I and  $\langle \text{Fe I} \rangle$  panels, the *horizontal dashed lines* are the unweighted mean values for old galaxies with  $\sigma > 150 \text{ km s}^{-1}$ .

compatible with first-ascent giant stars. The CO feature is too strong for these galaxies to be dwarf dominated.

At equivalent  $\sigma$ , the galaxies containing younger populations are separated from purely old galaxies. In the galaxies with purely old populations, NaI is highly correlated with  $\sigma$ , while CO and  $\sigma$  are less well-correlated. In contrast, neither CaI nor  $\langle \text{FeI} \rangle$  are well-correlated with  $\sigma$  –  $\langle \text{FeI} \rangle$  reaches a maximum value for  $\sigma \gtrsim 150$  while CaI has significant scatter at any given  $\sigma \gtrsim 150$ .<sup>2</sup>

Figure 14 shows the relationship between the optical index  $[\text{MgFe}]'$  and our new K-band index measurements.  $[\text{MgFe}]'$  is an abundance ratio insensitive optical index combination in the Lick system, designed to track total metallicity (Thomas, Maraston & Bender 2003). It is known to be well correlated with  $\sigma$ ; hence, it is not surprising that Figure 13 and Figure 14 look very similar for the purely old galaxies. Again, the galaxies that contain a young population are separated from the purely old galaxies at equivalent  $[\text{MgFe}]'$  and  $\sigma$ .

Figure 15 shows the relationships between various pairs of K-band spectral indices (compare to Figure 12). This figure captures several important observational conclusions already foreshadowed above:

- Relative to the observed cluster stars, the measured values of NaI are significantly stronger in the galaxies.
- In all cases, the galaxies that contain signatures of younger populations (i.e. stronger H $\beta$  and weaker  $[\text{MgFe}]'$ ) have stronger NaI and Fe features than comparable purely old galaxies.
- $\langle \text{FeI} \rangle$  saturates circa  $\sigma \sim 150 \text{ km s}^{-1}$  (NaI  $\sim 3.2$ ) in the same galaxies.

## 6. Discussion

No self-consistent theoretical spectral synthesis models for the interpretation of integrated K-band spectra of early-type galaxies are widely available. Development of such models is on-going (e.g. Marmol Queralt, 2007, in preparation). Until such models exist, we must rely on basic (and perhaps imperfect) astrophysical intuition and available tools, such as the high-resolution near-IR spectral atlas of Wallace & Hinkle (1996) (hereafter WK96).

---

<sup>2</sup>CaI is well-correlated with  $\sigma$  and  $[\text{MgFe}]'$  in purely old galaxies if NGC 1399 is removed from consideration. However, there is no sound reason for such data filtering at this time. Obviously, a larger sample is needed to investigate this issue.

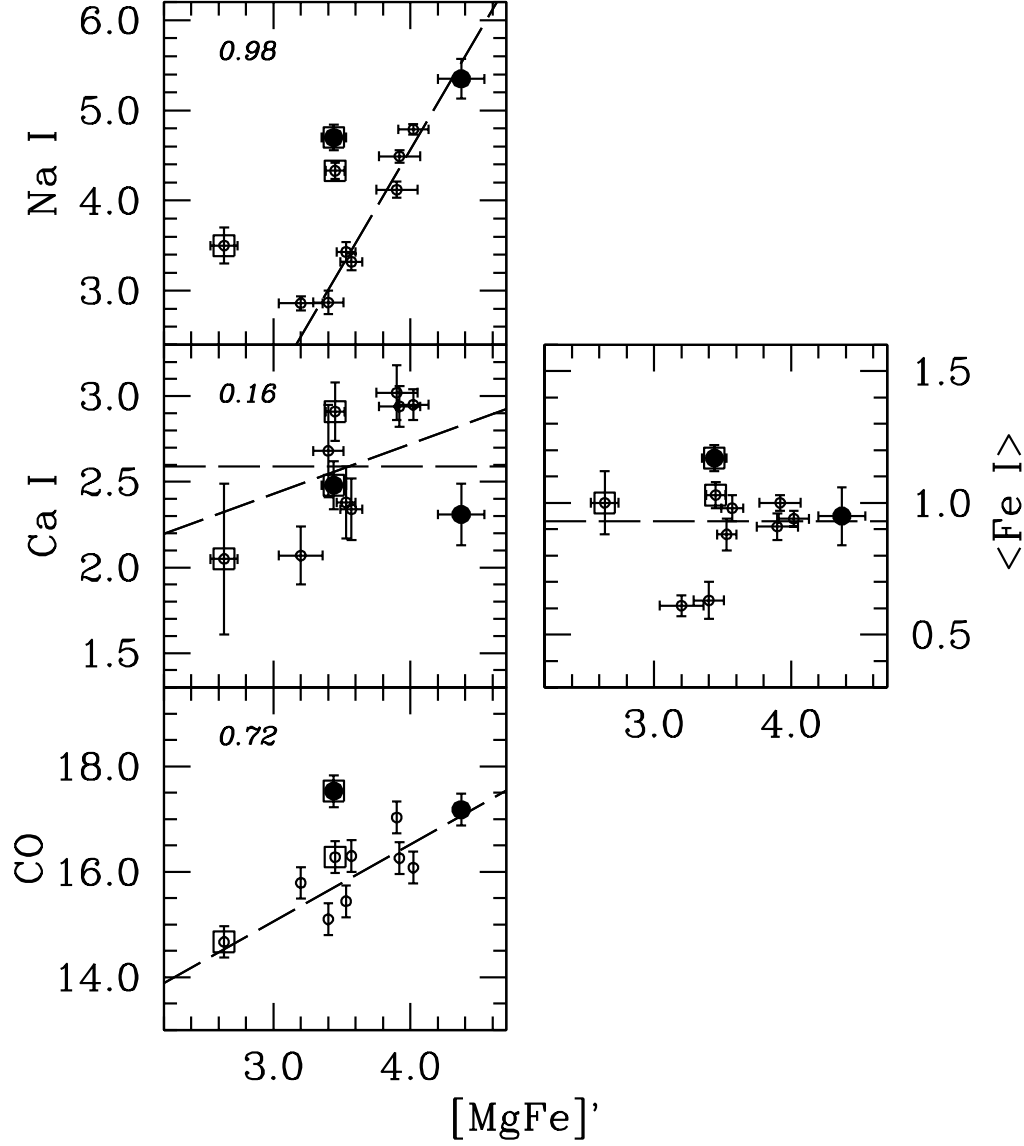


Fig. 14.— K-band feature strength vs.  $[MgFe]'$ .  $[MgFe]'$  is an optical index combination sensitive to total metallicity (Thomas, Maraston & Bender 2003). See Figure 13 for an explanation of symbol type and dashed line.

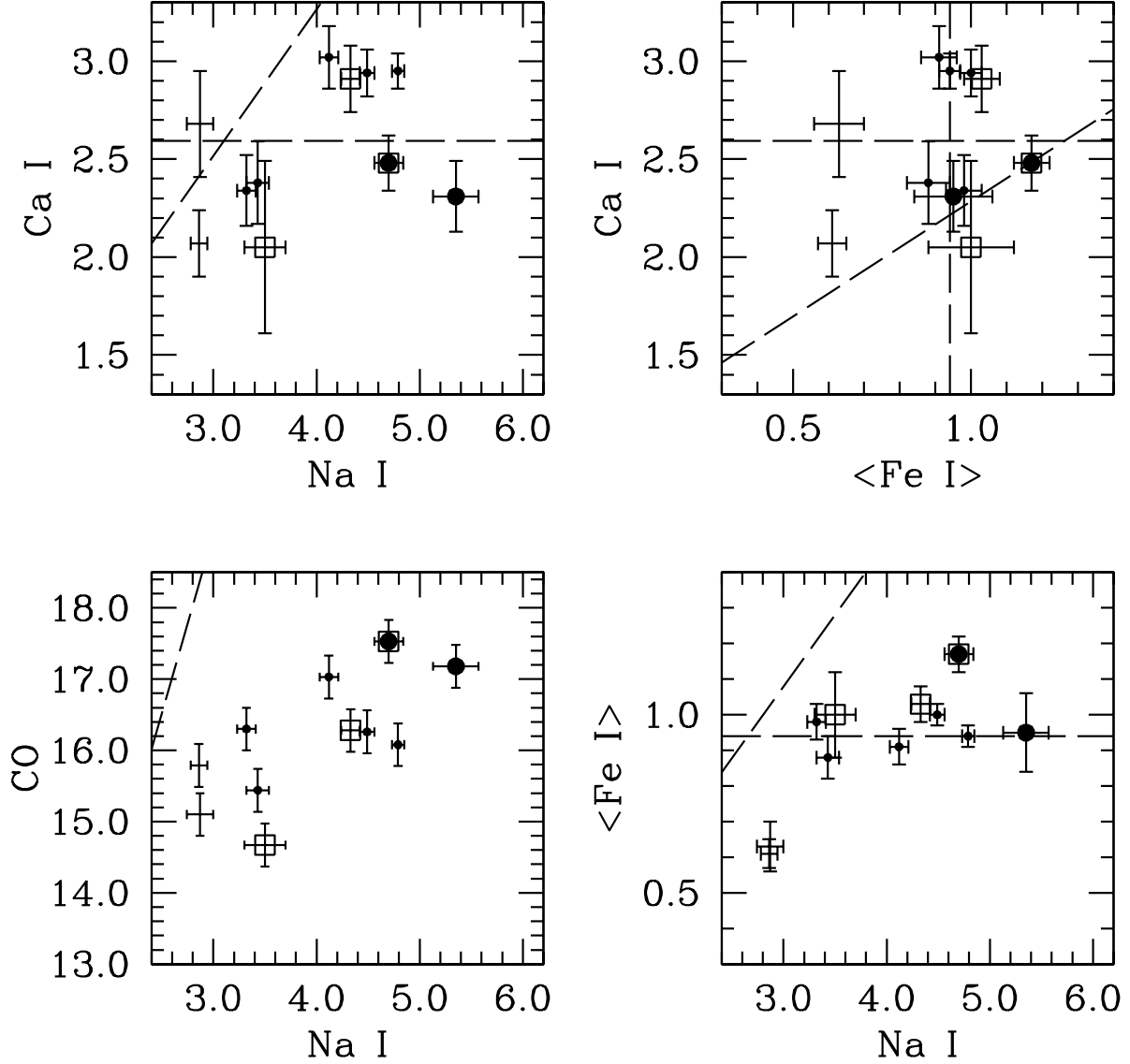


Fig. 15.— K-band index vs. index relationships. See Figure 13 for a symbol explanation. The *leftmost dashed line* in each figure are the cluster star fits shown in Figure 12. The *horizontal dashed lines* in the CaI and <FeI> panels are the mean values for purely old galaxies with  $\sigma > 150 \text{ km s}^{-1}$ . The *vertical dashed line* in the CaI vs. <FeI> panel is the mean <FeI> value.

### 6.1. Galaxies with young populations

Three galaxies in our sample (NGC 1316, NGC 1344, and NGC 1375) have stronger  $H\beta$  and weaker  $[MgFe]'$  features than the rest of our sample (see Figure 1). This suggests a simple, two component stellar population model. One stellar component is cold – in the luminosity-weighted mean, it is presumably old ( $> 8$  Gyr) and metal-rich ( $[Fe/H] > -0.3$ ) with spectral properties consistent with the observed central velocity dispersion. In other words, it has properties similar to the purely old galaxies in our sample (see Figure 1). The other component is warm – it contains a significant number of A/F dwarf or sub-giant stars. This component could have several origins but only two are considered here. Each has different consequences for K-band spectral index behavior.

First, the warm component could be associated with a young population with a warm ( $\sim 2 M_{\odot}$ ) main sequence turnoff (MSTO). The MSTO stars are tied to thermally pulsating asymptotic giant branch (TP-AGB) stars with bolometric magnitudes that place them above the tip of the first-ascent red giant branch (TRGB). The TP-AGB stars are cooler than stars on the first-ascent RGB and hence have an M spectral type. In the underlying luminosity function (spectral type vs. number of stars), the M-star bins are relatively more populated than in a purely old galaxy. The net effect is that integrated  $2.2 \mu m$  spectra should become more M-like.

Second, the warm component could be associated with a metal-poor population with a warm MSTO. These MSTO stars are tied to RGB stars with similar luminosity as the corresponding metal-rich RGB stars but with warmer  $T_{eff}$ . In the underlying luminosity function, the K-star bins will be relatively more populated than in a purely old population. The net effect is to make the integrated  $2.2 \mu m$  spectra more K-like.

Can the observations presented here distinguish between these two scenarios? Consider Figure 16 – the galaxies with relatively strong  $H\beta$  and weak  $[MgFe]'$  have relatively stronger (i.e. more M-like) near-IR features. Qualitatively, this is consistent with the first scenario. Can this conclusion be better quantified? What is the relative ratio of young to old stellar mass? Are the changes in optical and near-IR spectral features *quantitatively* consistent?

To begin to answer these questions, the Thomas et al. (2003) models were used to create very simple two-component models that produced optical index values that matched the observed values in the three galaxies with strong  $H\beta$ . One component was old (11 Gyr) with metallicity set to  $[Z/H] = 0.35$  for NGC 1316 and NGC 1344 and 0.0 for NGC 1375. The other component had the same metallicity but a young (1 Gyr) age. The relative mass fractions of these components were varied until the model  $H\beta$  strength matched the observed  $H\beta$  strength. The resultant young mass fractions (where total mass = 1) were 0.135, 0.075,

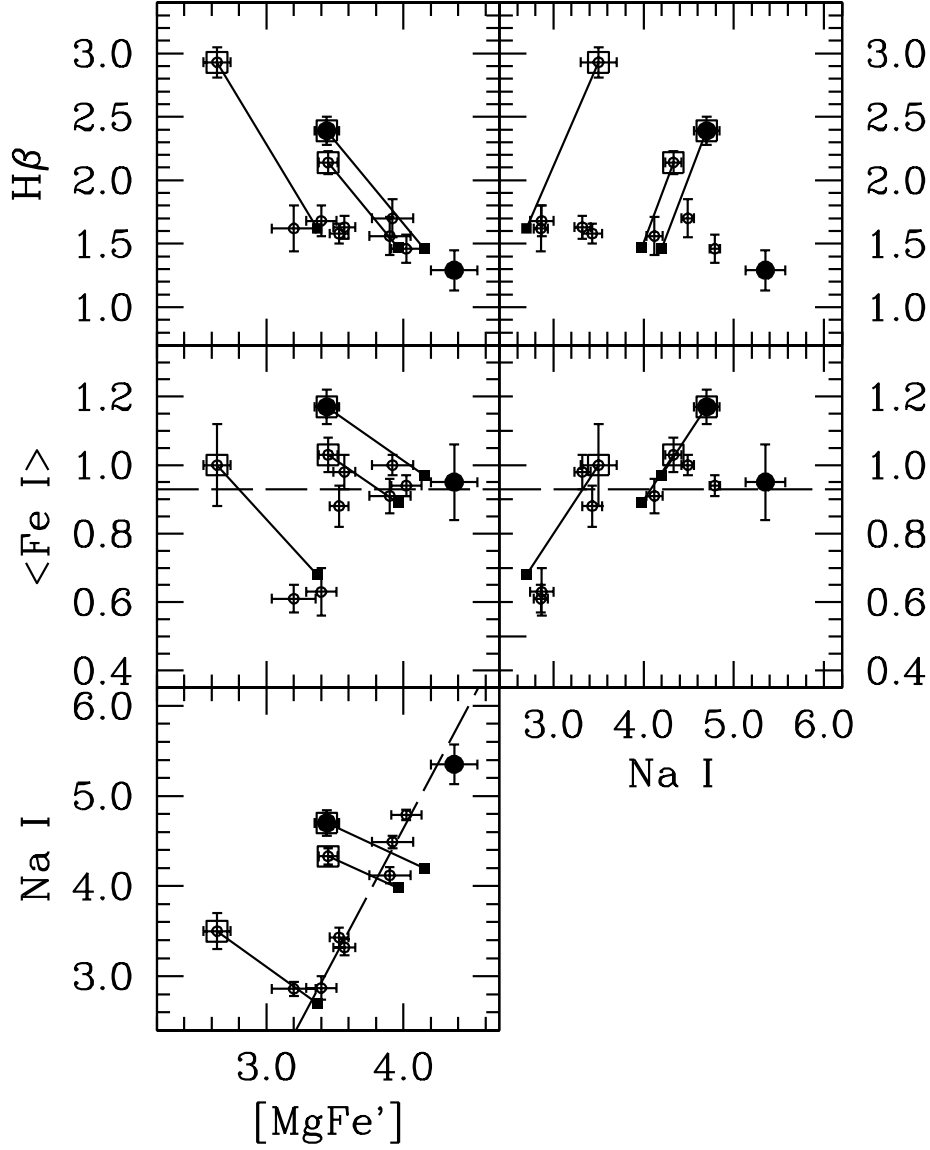


Fig. 16.— Optical-NIR corrections for young populations. See Figure 13 for a symbol explanation. The observed index strengths for the galaxies with young components are connected to the predicted index strengths (*solid squares*) after the effects of a young component has been removed. In the lower panel, the *slanted dashed line* indicates the unweighted linear regression fit for the purely old galaxies with  $\sigma > 150 \text{ km s}^{-1}$ . In the middle panels, the *horizontal dashed line* indicates the unweighted mean value for purely old galaxies with  $\sigma > 150 \text{ km s}^{-1}$ .

and 0.140 for NGC 1316, NGC 1344, and NGC 1375, respectively. The implied differential correction between the purely old model and the two-component model was then applied to the observed data (see Figure 16).

Next, observed  $\langle \text{Fe I} \rangle$  strength was adjusted manually until all three galaxies lay within the locus of purely old galaxies with similar  $\sigma$  in the  $\langle \text{Fe I} \rangle$  vs. Na I panel. As part of this adjustment,  $\Delta(\langle \text{Fe I} \rangle)/\Delta(\text{Na I})$  was forced to agree with the value (0.62) determined for the observed Galactic cluster giant stars (see Figure 12). This is a trend in effective temperature that is relatively insensitive to metallicity. Cooler giant stars (more late K and early M like) have strong K-band spectral features.

In addition to the  $\Delta(\langle \text{Fe I} \rangle)/\Delta(\text{Na I})$  measured from the Galactic open cluster stars, two other key numerical trends can be computed:

$$\Delta(\langle \text{Fe I} \rangle)/\Delta(\text{Na I}) = 0.62 \quad (2)$$

$$\Delta(\text{Na I})/\Delta([\text{MgFe}]') = 0.70(1.10) \quad (3)$$

$$\Delta(\langle \text{Fe I} \rangle)/\Delta([\text{MgFe}]') = 0.28(0.44) \quad (4)$$

NGC 1316 and NGC 1344 could be forced to have consistent trajectories. However, NGC 1375 (values shown in parenthesis) appears to follow somewhat different trajectories. Obviously, this kind of cartoon model is illustrative only and surely hides a plethora of details. Indeed, the real trajectories are unlikely to be linear. Nevertheless, a clear astrophysical conclusion emerges: for the  $\text{H}\beta$ -strong galaxies, the observed optical and near-IR features all change in concert, consistent with a warm MSTO tied to an extended RGB, which is in turn consistent with the presence of a young stellar component, not a metal-poor stellar component.

## 6.2. Galaxies with bright K-band SBF

Liu, Graham, & Charlot (2002) found that relative I-band and K-band surface brightness fluctuation strength (expressed as an SBF color,  $\bar{I} - \bar{K}$ ) was essentially constant for the majority of the early-type galaxies they studied in Fornax. However, two galaxies in common with our sample (NGC 1419 and 1427) were found to have brighter (larger) K-band SBF relative to the mean relationship (see also Mei et al. 2001). A larger  $\bar{K}$  is thought theoretically to arise from the presence of an extended giant branch, i.e. more cool, bright, M giants.



In the spectroscopic data discussed here, there are no indications of such extended giant branches in these galaxies – their central line indices are consistent with an integrated stellar populations dominated by an old, metal-rich population. Of course, the SBF measurements were made in the outer regions of these galaxies, as opposed to the optical and near-IR observations of the central regions discussed here. It may be that the integrated luminosity of such a component (if present at all) is not high enough in the central region for detection by our method.

### 6.3. Purely old galaxies

In purely old galaxies, we have seen that:

- NaI is stronger than in Galactic open clusters and is highly correlated with  $\sigma$  and  $[\text{MgFe}]'$ .
- $\langle \text{FeI} \rangle$  saturates for  $\sigma \gtrsim 150 \text{ km s}^{-1}$ .
- CO is somewhat correlated with  $\sigma$  and  $[\text{MgFe}]'$ , while CaI is not (unless NGC 1399 is not included in the regression fits, see footnote 2 above).

The observed K-band spectral features are named for the dominant elemental species in the *solar* spectrum. However, at the effective temperatures of interest here, the on-band index definition and their companion off-band continuum bands contain lines from other elemental species as well (as Ramirez et al. 1997 discuss comprehensively). By referring to the high resolution spectra of WK96, the contribution from these other absorbers can be investigated and used to explain the overall spectral feature behavior. In turn, underlying astrophysical parameters related to galaxy formation and evolution are revealed.

#### 6.3.1. NaI index

In the current galaxy sample, NaI is significantly stronger than observed in the Galactic open cluster stars. The off-bands defined for the NaI feature are relatively line-free, so we can focus on the on-band spectral region (see the  $\lambda$  Dra, M0 III spectrum in WK96, p. 352). In addition to sodium, Sc, Si, and (to a lesser extend) V are significant absorbers in this region. Origlia et al. (1997) argued that  $[\text{Si/Fe}]$  is super-solar in a small sample of early-type galaxies based in measurements of the Si I  $1.59 \mu\text{m}$  feature. Trager et al. (2000) have argued that both  $[\text{Na/Fe}]$  and  $[\text{Si/Fe}]$  are super-solar in early-type galaxies based on

models of optical spectral feature behavior. The K-band NaI measurements presented here are consistent with enhanced silicon in the observed Fornax galaxies and hence indirectly confirm the conclusions of Origlia et al. and Trager et al.

### 6.3.2. $\langle \text{Fe I} \rangle$ index

The Fe I A feature contains approximately equal absorption contributions from Fe, Sc and Ti while Fe I B is dominated by Fe absorption features with some additional Sc absorption (in WK96, see the  $\lambda$  Dra, M0 III spectra on p. 346 and 348). Hence, the  $\langle \text{Fe I} \rangle$  index (a combination of Fe I A and Fe I B) is dominated by absorption lines from Fe-peak elements). For purely old galaxies with  $\sigma > 150 \text{ km s}^{-1}$ ,  $\langle \text{Fe I} \rangle$  is observed to remain constant while NaI (an index dominated by absorption lines from  $\alpha$ -elements) and  $[\text{MgFe}]'$  (a total metallicity  $[\text{Z}/\text{H}]$  indicator) become stronger as  $\sigma$  increases. It is tempting to conclude that above  $\sigma > 150 \text{ km s}^{-1}$  luminosity-weighted mean total metallicity  $[\text{Z}/\text{H}]$  continues to increase as a function of central velocity dispersion, driven by a relative increase of  $[\alpha/\text{H}]$ , while  $[\text{Fe}/\text{H}]$  remains constant.

However, within the narrow  $[\text{Fe}/\text{H}]$  range of observed Galactic open cluster stars,  $\langle \text{Fe I} \rangle$  is more strongly correlated with effective temperature than cluster  $[\text{Fe}/\text{H}]$  (see Figure 10). Increasing mean total metallicity  $[\text{Z}/\text{H}]$  in the galaxies should correspond to cooler mean RGB effective temperature and hence increased  $\langle \text{Fe I} \rangle$ . Recall that the relationship between  $\langle \text{Fe I} \rangle$  and mean RGB effective temperature has already been exploited above to explain the observed behavior of  $\langle \text{Fe I} \rangle$  (and NaI) in galaxies with young stellar components. The dilemma is clear: how can a temperature-sensitive index like  $\langle \text{Fe I} \rangle$  remain constant while mean RGB effective temperature decreases due to increasing  $[\text{Z}/\text{H}]$ ?

Without appropriate population synthesis models or stellar spectra, only a few speculative thoughts can be offered. In their detailed comparison of non-solar abundance population synthesis models with measurements of spectral indices in the optical Lick system, Trager et al. (2000) concluded that their best-fit models included enhancements in C, N, Na, and Si (among others). As  $[\alpha/\text{H}]$  increases with  $\sigma$  (as suggested by increasing NaI), stronger CN bands in the Fe I A and Fe I B on-band and off-band windows (see the WK96 spectra referenced above and the band definitions in Table 6) may have the effect of depressing the local continuum and hence decreasing the value of  $\langle \text{Fe I} \rangle = (\text{Fe I A} + \text{Fe I B})/2$ . For example, Trager et al. noted a similar effect from  $\text{C}_2$  bands in the optical Mg  $b$  index. Therefore, it may be that above some critical mean  $[\alpha/\text{H}]$  and below some critical mean effective temperature,  $\langle \text{Fe I} \rangle$  stays within a narrow range and provides no useful information about mean  $[\text{Z}/\text{H}]$ ,  $[\text{Fe}/\text{H}]$ , or effective temperature.

A conclusive astrophysical explanation of  $\langle \text{FeI} \rangle$  in early-type galaxies with  $\sigma > 150 \text{ km s}^{-1}$  awaits larger galaxy samples, observations of appropriate stars (e.g. in the Galactic bulge), and detailed population synthesis models.

### 6.3.3. CO index

The CO feature is dominated by the  $^{12}\text{CO}(2,0)$  bandhead and has no significant absorption components from other elements. Like  $\langle \text{FeI} \rangle$  above, CO is highly correlated with  $T_{eff}$  in the observed Galactic open cluster stars and reaches larger values than observed in the galaxies. As a function of central velocity dispersion  $\sigma$  in the observed galaxies, CO does not appear to saturate (or at least not as definitively as  $\langle \text{FeI} \rangle$ ). This adds credence to the suspicion that  $\langle \text{FeI} \rangle$  is not tracing mean RGB effective temperature in galaxies with  $\sigma > 150 \text{ km s}^{-1}$ . Based on the current measurements, no conclusions can be reached about relative carbon or oxygen abundance in these galaxies.

### 6.3.4. CaI index

No obvious explanation presents itself for the behavior of CaI in this galaxy sample. The CaI feature is intrinsically complex, consisting of contributions from many absorbers: Ca, S, Si, and Ti (all  $\alpha$ -elements) as well as Sc and Fe (see  $\lambda \text{ Dra}$ , MO III spectrum in WK96, p. 342). As a function of  $T_{eff}$  in the range of interest, some of the contributing absorption lines get stronger (Sc and Ti, the former faster than the latter), some features get weaker (Si), and some remain roughly constant (Ca, S, and Fe) (cf. Ramirez et al. 1997). Relative to solar abundance ratios, Trager et al. (2000) have argued that Si and S are over-abundant and Ca is under-abundant in early-type galaxies while  $[\text{Ti}/\text{Fe}]$  and  $[\text{Sc}/\text{Fe}]$  have their solar values. In the Galactic open cluster stars observed here, the CaI feature is stronger at a given  $J - K$  ( $T_{eff}$ ) in the solar-metallicity stars than in the more metal-poor stars. Within the galaxies observed here, CaI appears to have significant scatter at any given  $\sigma$  or  $[\text{MgFe}]'$ . No obvious explanation for this scatter (or the global behavior of CaI with  $\sigma$  and  $[\text{MgFe}]'$ ) presents itself at this time.

## 7. Summary

Using new, moderate resolution ( $R \sim 2500$ ) K-band spectra, spectral indices have been measured in the central regions of eleven early-type galaxies in the nearby Fornax cluster.

Based on these measurements, the following conclusions were reached:

1. The NaI feature is much stronger in these Fornax early-type galaxies than observed in solar-metallicity Galactic open cluster stars. This is attributed to relative [Si/Fe] (and possible [Na/Fe]) differences between the open cluster stars and the Fornax galaxies, i.e. both are larger in the Fornax galaxies than in the cluster stars.
2. In various near-IR diagnostic diagrams, galaxies with optical indices indicative of a warm stellar component are clearly separated from galaxies dominated by colder, presumably old ( $\geq 8$  Gyr) stellar populations. Changes in the near-IR spectra features are consistent with the presence of an cool component dominated by late K and/or early M giants stars. In combination, the optical and near-IR observations are consistent with the presence of a young stellar component with a warm MSTO and a significant extended giant branch consisting of TP-AGB stars.
3. For detecting a young stellar component, the NaI vs.  $\sigma$  or  $\langle \text{FeI} \rangle$  vs.  $\sigma$  diagnostic diagram seems as efficient as using  $\text{H}\beta$  vs.  $[\text{MgFe}]'$  (or other similar combinations of optical indices). The near-IR features have the additional advantage that no emission-line correction is needed (as it is necessary for the stronger optical Balmer lines).
4. The  $\langle \text{FeI} \rangle$  index saturates in galaxies with central velocity dispersion  $\sigma > 150 \text{ km s}^{-1}$  dominated by old ( $\geq 8$  Gyr) stellar populations. For  $\sigma > 150 \text{ km s}^{-1}$ , these Fe features are unlikely to be useful for investigating stellar population differences between early-type galaxies. Above  $\sigma > 150 \text{ km s}^{-1}$ , the continued increase in NaI (and  $[\text{MgFe}]'$ ) strength with  $\sigma$  coupled with constant  $\langle \text{FeI} \rangle$  presents an astrophysical challenge. Although it is tempting to conclude that  $[\text{Fe}/\text{H}]$  reaches a maximum value, while  $[\alpha/\text{H}]$  (and hence  $[\text{Z}/\text{H}]$ ) continues to increase, more observational and population synthesis work is needed to understand conclusively the behavior of  $\langle \text{FeI} \rangle$  in these high-mass early-type galaxies.

Adding these near-IR indices to the standard diagnostic toolkit for analyzing the integrated light of early-type galaxies clearly has great potential. To develop this potential, three obvious steps are needed: observe more galaxies over a larger range of central velocity dispersion (including field galaxies with existing optical data) and extend current population synthesis models to the near-IR. We know that various groups are working on both steps. It would also be useful to study the radial behavior of these indices within individual galaxies to compare and contrast index behavior between galaxies.

For the foreseeable future, the study of the central populations in early-type galaxies will remain the study of integrated light. As distance increases, our ability to study the

central regions of early-type galaxies within metric apertures equivalent to nearby galaxies relies on the high *spatial* resolution spectroscopy achievable from space or with adaptive optics on the ground. In the former case, the James Webb Space Telescope represents the frontier – yet, no optical spectrograph that works below  $0.8\ \mu\text{m}$  is currently planned. In the latter case, the frontier will be shaped by further development of adaptive optics systems – and these systems will achieve their best performance beyond  $1\ \mu\text{m}$ . Hence, understanding how to interpret near-IR spectral indices in nearby galaxies is key to facilitating the kind of investigation and characterization of more distant early-type galaxies that will not be possible at optical wavelengths.

We thank the anonymous referee for a quick, enthusiastic, and helpful review that drove us to clarify several key points. This research has made use of the NASA/IPAC Extragalactic Database (NED) which is operated by the Jet Propulsion Laboratory, California Institute of Technology, under contract with the National Aeronautics and Space Administration. This research has also made use of the SIMBAD database, operated at CDS, Strasbourg, France. Thanks to Valentin Ivanov and Olivier Marco for observing assistance during the acquisition of the ISAAC data. DRS warmly thanks ESO Santiago for hospitality during July 2003 science leave, especially Danielle Alloin, during which much of these data were processed. We acknowledge various helpful discussions with Andrew Stephans, Daniel Thomas, Claudia Maraston, Scott Trager and Guy Worthey on topics related to stellar populations in early-type galaxies. Thanks to Chris Lidman and Rachael Johnson for various discussions about reducing ISAAC spectroscopic data. Many of the science and technology concepts in this paper grew out of late night conversations between DRS and Richard Elston (1961 – 2004) – friend, colleague, fellow observer — while we were both postdocs at Kitt Peak. Richard — thanks.

*Facilities:* VLT:Antu (ISAAC) VLT:Yepun (SINFONI)

## REFERENCES

- Alloin, D., & Bica, E. 1989, *A&A*, 217, 57
- Bonnet, H. et al. 2004, *The ESO Messenger*, 117, 17
- Caon, N., Capaccioli, M., & D’Onofrio, M. 1994, *A&AS*, 106, 199
- Cappellari, M., & Emsellem, E. 2004, *PASP*, 116, 138
- Carter, D., Visvanathan, N., & Pickles, A.J. 1986, *ApJ*, 311, 637

- de Carvalho, R. R., da Costa, L. N., & Djorgovski, S. 1991, ApJS, 76, 1067
- da Costa, L.N. et al. 1998, AJ, 116, 1
- de Carvalho, R. R., da Costa, L. N., & Djorgovski, S. 1991, ApJS, 76, 1067
- Delisle, S., & Hardy, E. 1992, AJ, 103, 711
- Devillard, N., 1997, The ESO Messenger, 87, 1
- D’Onofrio, M. et al. 1995, A&A, 296, 319
- Eisenhauer, F. et al. 2003 in *Instrument Design and Performance for Optical/Infrared Ground-based Telescopes*, eds. Iye, M. & Moorwood, A., Proceedings of the SPIE, 4841, 1548
- Förster Schreiber, N. M. 2000, AJ, 120, 2089
- Frogel, J. A., Stephens, A., Ramírez, S., & DePoy, D. L. 2001, AJ, 122, 1896
- Ferguson, H.C. 1989, AJ, 98, 367
- Graham, A.W. et al. 1998, A&AS, 133, 325
- Houdashelt, M.L., Frogel, J.A., & Cohen, J.G. 1992, ApJ, 103, 163
- James, P. A., & Mobasher, B. 1999, MNRAS, 306, 199
- James, P. A., & Mobasher, B. 2000, MNRAS, 317, 259
- Johnson, H.L. 1966, ARA&A, 4, 193
- Kuntschner, H. 2000, MNRAS, 315, 184
- Kuntschner, H., Smith, R. J., Colless, M., Davies, R. L., Kaldare, R., & Vazdekis, A. 2002, MNRAS, 337, 172
- Kuntschner, H. 2004, A&A, 426, 737
- Lee, T.A. 1970, ApJ162, 217
- Liu, M.C., Graham, J.R., & Charlot, S. 2002, ApJ, 564, 216
- Longo, G., Zaggia, S.R., Busarello, G., & Richter, G. 1994, A&AS, 105, 433
- Malin, D.F., & Carter, D. 1980, Nature, 285, 643

- Maraston, C., & Thomas, D. 2000, ApJ, 541, 126
- Mei, S., Kissler-Patig, M., Silva, D.R., & Quinn, P.J. 2001, A&A, 371 779
- Mobasher, B., & James, P. A. 1996, MNRAS, 280, 895
- Mobasher, B., & James, P. A. 2000, MNRAS, 316, 507
- Origlia, L., Ferraro, F.R., Fusi Pecci, F., & Oliva, E.,  $\alpha$ , 321, 859
- Ramírez, S.V., DePoy, D.L., Frogel, J.A., Sellgren, K., & Blum, R.D. 1997, AJ, 113, 1411
- Silva, D. R., Boroson, T. A., Elston, R., & Rich, R. M. 1994, Astronomy with Arrays, The Next Generation, 190, 525
- Silva, D.R. & Bothun, G.D. 1998a, AJ, 116, 85
- Silva, D.R. & Bothun, G.D. 1998b, AJ, 116, 2793
- Stoehr, F., et al. 2007, Space Telescope European Coordinating Facility Newsletter, 42, 4
- Thomas, D., Maraston, C., & Bender, R. 2003, MNRAS, 339, 897
- Trager, S. C., Faber, S. M., Worthey, G., & González, J. J. 2000, AJ, 119, 1645
- Trager, S. C., Worthey, G., Faber, S. M., & Dressler, A. 2005, MNRAS, 362, 2
- de Vaucouleurs, G. et al. 1991, *Third Reference Catalogue of Bright Galaxies*.
- Wallace, L., & Hinkle, K. 1996, ApJS, 107, 312
- Wallace, L., & Hinkle, K. 1997, ApJS, 111, 445
- Worthey, G., Faber, S. M., Gonzalez, J. J., & Burstein, D. 1994, ApJS, 94, 687